Carbohydrate Polymers 284 (2022) 119202

Contents lists available at ScienceDirect

Carbohydrate Polymers

journal homepage: www.elsevier.com/locate/carbpol

# Functionalized chitosan/spherical nanocellulose-based hydrogel with superior antibacterial efficiency for wound healing

Dinesh K. Patel [a,1], Keya Ganguly [a,1], Jin Hexiu [b,1], Sayan Deb Dutta [a], Tejal V. Patil [c], Ki-Taek Lim [a,c,*]

[a] Department of Biosystems Engineering, Institute of Forest Science, Kangwon National University, Chuncheon 24341, Republic of Korea
[b] School of Stomatology, Capital Medical University, Beijing 100050, China
[c] Interdisciplinary Program in Smart Agriculture, Kangwon National University, Chuncheon 24341, Republic of Korea

ARTICLE INFO

*Keywords:*
Carboxymethyl chitosan
Nanocellulose
Injectable hydrogel
Adhesive
Recoverable
Biocompatibility
Wound healing

ABSTRACT

Cellulose nanomaterials have received significant interest due to their superior physicochemical properties and biocompatibility. The nanomaterials-based hydrogel patches are widely explored for skin regeneration. However, the injectability and adhesiveness of the hydrogels are crucial challenges for tissue engineering applications. To overcome these, we synthesized an injectable and adhesive hydrogel of spherical nanocellulose (s-NC) reinforced carboxymethyl chitosan for rapid skin regeneration. The s-NC exhibited improved cellular activity than cellulose nanocrystals. The hydrogels exhibited adhesive and injectability potentials and were molded in the desired configurations. An enhanced conductivity was observed in s-NC added hydrogels than the pure polymer hydrogel. The skin regeneration potential of the hydrogel scaffolds was also examined in the rats using the wound healing model. The composite scaffolds also showed improved antibacterial potential. Taken together, the developed hydrogels have the potential and can be explored as a promising biomaterial for enhanced skin regeneration applications.

## 1. Introduction

Skin is the largest organ in vertebrates, acting as the outermost barrier between the body and the surrounding environment. It comprises the epidermal, dermal, and hypodermal layers with a typical thickness of 0.5–4 mm (Keirouz et al., 2020). It plays a vital role in preventing body damage from different aspects, including chemical and mechanical factors (Brandner et al., 2013). The loss of the skin's structural integrity, which may be due to burns, abrasion, ulcers, and lesions, causes a wound. It is difficult to achieve complete skin recovery *via* skin grafts because of the limited and fewer donor sources and antigenicity of the donor tissue (Ma, 2003; Schauber et al., 2012). Different pharmacological, physical, and phytotherapeutic approaches have been utilized to improve skin recovery (Corin & Gibson, 2010; Dainiak et al., 2010). Tissue engineering approaches have received considerable attention for the repair and regeneration of damaged tissues; wherein a structure is developed to mimic the native environment of the extracellular matrix (ECM) (Lukanina et al., 2018). The developed structures need to be biocompatible, biodegradable, and appropriately porous to improve cell growth, differentiation, adhesion, and migration (Wang et al., 2015). Electrospinning, solvent casting, gas foaming, melt molting, freeze-drying, and 3D-printing approaches have been applied to fabricate porous scaffolds for different applications (Mabrouk et al., 2020). Different materials, including alginate, chitosan, gelatin, collagen, poly (caprolactone), poly(lactic acid), and poly(lactic-*co*-glycolic acid), have been widely explored for tissue engineering applications because of their superior physicochemical properties (Blackstone et al., 2018; Pal et al., 2017; Yu et al., 2019).

It is well known that skin is electrical sensitive and has an electrical conductivity from 2.6–1 $\times$ $10^{-4}$ mS, depending on the skin tissue constituents (Korupalli et al., 2020; Zhao et al., 2018). Therefore, it is anticipated that the electroactive materials with similar conductivity and adhesiveness potential will facilitate rapid wound healing. The adhesiveness property enables closed contact of the implanted materials with the defected tissue without using other substrates. Chitosan (CS), a deacetyl-derivative of chitin, has received more attention in tissue engineering applications because of its excellent biocompatibility and biodegradability (Wu et al., 2018). CS acts as a cationic polyelectrolyte, and its membrane has been explored to transport the active ions in

* Corresponding author at: Interdisciplinary Program in Smart Agriculture, Kangwon National University, Chuncheon 24341, Republic of Korea.
*E-mail address:* ktlim@kangwon.ac.kr (K.-T. Lim).
[1] Equal contributions

https://doi.org/10.1016/j.carbpol.2022.119202
Received 25 November 2021; Received in revised form 28 January 2022; Accepted 28 January 2022
Available online 1 February 2022

**Nomenclature**

| | |
|---|---|
| CMCS | Carboxymethyl chitosan |
| DMEM | Dulbecco Modified Eagle Medium |
| ICR | Institute of Cancer Research |
| PECAM-1 | Platelet endothelial cell adhesion molecule-1 |
| CD 31 | Cluster of differentiation 31 |
| VEGF | Vascular endothelial growth factor |
| VE-cadherin | Vascular endothelial-cadherin |

aqueous conditions (Wan et al., 2003). However, the ionic conductivity of CS film under the dry condition is limited and can be enhanced by adding aqueous media or conducting nanomaterials (Croisier & Jérôme, 2013).

The rapid growth of the bacteria occurred nearby the defective area, which significantly restricted the wound healing process. Therefore, the materials which can absorb the wound exudates and reduce bacterial growth are favorable for wound healing application (Khodabakhshi et al., 2019; Yuan et al., 2019). CS has poor water solubility and exhibited low antibacterial at a higher pH (< 6.5). Thus, its broad applicability is restricted within acidic conditions (Wu et al., 2021). Therefore, modifications are required to overcome these challenges. Carboxymethyl chitosan (CMCS), a water-soluble polysaccharide, is considered an attractive material for tissue engineering because of its superior physicochemical and retention of CS properties (Luo et al., 2018). Rapid angiogenesis is a crucial challenge for skin regeneration. Different approaches, including encapsulation of specific genes, the addition of angiogenic promoting factors, such as vascular endothelial growth factor, basic fibroblast growth factor, and platelet-derived growth factor, or co-culture with different cells, have been explored for improved skin regeneration (Wang et al., 2015). CS promoted cell proliferation and migration and accelerated angiogenesis during wound healing (Lord et al., 2017).

Cellulose is one of the most abundant biopolymers produced on earth and is extensively used in the paper, energy sources, textiles, and clothing industries (Domingues et al., 2014). It comprises $_{D}$-glucose units linked by $\beta$-1, 4 glycosidic bonds (Azizi Samir et al., 2005). Cellulose is an essential component of the plant cell wall and is connected *via* hydrogen bonds and van der Waals forces that form fibrillar structures. These fibrils are further assembled to form microfibrils with an average diameter of 5–50 nm and lengths of several micrometers. Nanoscale cellulose, called nanocellulose, has attracted significant attention for its use as a filler material because of its excellent physicochemical properties, such as high surface area, aspect ratio, superior mechanical and optical properties, and biocompatibility (Patel et al., 2019a). Cellulose nanocrystals (CNCs)/spherical nanocellulose (s-NC), nanofibrillated cellulose (NFC), and bacterial nanocellulose (BNC) are considered nanostructured cellulose (Luo et al., 2019). CNCs have a crystalline and needle-like morphology with typical widths and lengths of 20 nm and 100–250 nm, respectively (Xu et al., 2013). The wound healing potential of the CS and modified CS has been earlier reported (Alavi & Nokhodchi, 2020; Cardoso et al., 2019; Liu et al., 2018). Xie et al. showed improved antibacterial and wound healing potential of silver nanoparticles-loaded chitosan hydrogels (Xie et al., 2018). However, the development of multifunctional integrated hydrogels without using the growth factors or metal ions has remained a critical challenge in tissue engineering.

We developed the multifunctional integrated hydrogels of CMCS/s-NC to overcome these issues for rapid wound healing. The recovery strength, swelling, and degradation potentials were examined. The biocompatibility of the developed hydrogel scaffolds was investigated using a co-culture of human dermal fibroblast (HDF), human keratinocyte (HaCaT), and human umbilical vein endothelial cell (HUVEC) *via* the WST-8 assay, *in vitro*. The conductivity and antibacterial potentials were also monitored. Finally, the wound healing process was assessed using the rats after 14 days of the scaffolds implantation. Therefore, we hypothesize that the hydrogel scaffolds developed from polysaccharides positively affects skin cell proliferation and can be explored in skin tissue engineering for rapid wound closure.

## 2. Experimental sections

### 2.1. Materials

The high molecular weight chitosan powder (310–375 kDa, >75% deacetylated) potassium hydroxide (both from Sigma Aldrich, USA), sodium chlorite, ammonium persulfate (APS) (Daejung Chemicals, Republic of Korea), acetic acid (99.7%), hydrochloric acid (35%), sulfuric acid (98.08%) (mass/mass, Wako Chemicals, Republic of Korea), and sodium hydroxide (Junsei Chemicals, Japan) were used in this work. The WST-8 dye was purchased from the Cellrix® (MediFab Co., Ltd. Republic of Korea). All chemicals were used as received from the supplier.

### 2.2. Nanocellulose extraction and synthesis of water-soluble CMCS

The extraction of s-NC and CNCs was performed from pine wood powder through chemical treatment, and the detailed processes are given in Supplementary Information (SI). The CMCS was synthesized as earlier reported somewhere else (Luo et al., 2018). Briefly, a known amount of CS was added in 50% sodium hydroxide solution and kept in a refrigerator for 24 h, followed by adding the required amounts of isopropanol with continuous mechanical stirring. After that, the calculated amounts of monochloroacetic acid were added to the reaction mixture and stirred at 60 °C for 6 h, then filtered and washed with ethanol. The obtained sample was dissolved in distilled water and dialyzed for three days. The dialyzed sample was concentrated by a rotary evaporator and a freeze-dried by freeze dryer (EYELA® Freeze Drying Unit 2200, Tokyo, Japan).

### 2.3. Synthesis of CMCS and CMCS/s-NC composite hydrogel scaffolds

The hydrogels were prepared by dissolving the required amounts of CMCS (5%, *w/w*) in distilled water. The composite hydrogels were prepared by adding the different amounts of s-NC (1, 2, and 4%, *w/w*, w.r.t. CMCS) in the CMCS matrix. The developed hydrogels were precooled at −80 °C for 6 h, followed by freeze-drying to prepare the porous scaffolds. The pure polymer and composite hydrogel scaffolds were designed as CMCS, and CMCS/s-NC X, where X is the amount of s-NC in the CMCS matrix.

### 2.4. Spectroscopic characterization of hydrogel scaffolds

The Fourier transform infrared (FTIR) spectroscopy (Frontier, Perkin Elmer, UK) was used to monitor the functional groups in s-NC and their interaction with CMCS matrix in the range of 4000–400 $cm^{-1}$ with a resolution of 4 $cm^{-1}$. The number of scans was 64 in FTIR measurement. Transmission electron microscopy (TEM) (JEM, 2100 F, Jeol, Japan) was employed to measure the size and morphology of s-NC. The synthesized CMCS was characterized by the proton nuclear magnetic resonance (NMR) spectroscopy (Bruker Avance Neo 600) in $D_2O$ as solvent at 80 °C. The surface morphologies of the developed hydrogel scaffolds were examined by scanning electron microscopy (SEM) (S-4800, Tokyo, Japan). The structural changes in the scaffolds were evaluated by X-ray diffractometer (X'Pert PRO MPD, Philips, Eindhoven, Netherlands) at operating voltage and current of 40 kV and 40 mA, with Cu Kα radiation (λ = 1.5414 A°). The operating range (2θ) was 5–40°. The rheological properties of the developed hydrogels were evaluated by an ARES-G2 rheometer (TA Instrument, New Castle, Delaware, USA) with a 6 mm parallel plate at 25 °C.

### 2.5. Recovery, injectability, and adhesive abilities of hydrogels

The recovery potential of the developed hydrogels was evaluated by measuring the viscosity *via* an ARES-G2 rheometer with different shear rates (0.1, 100, and 0.1 $s^{-1}$) for different time intervals (0–100, 101–200, and 201–300 s), at 25 °C, respectively. The injectability property was assessed using a 10 mL syringe with a needle dimension of 21G.

The lap shear test was performed to quantify the adhesive strength between a hydrophobic surface (plastic) and the developed hydrogel after 20 min of treatment by uniaxial tensile measurement. For this, 200 μL of the developed hydrogels were placed on the plastic surface to cover an area of 25 mm × 15 mm. The second plastic sheet was placed over the adhesive layer and left for the desired time at room temperature. After that, the uniaxial tensile measurement was performed to measure the adhesive strength of the hydrogels. All experiments were accomplished in triplicate ($n = 3$).

### 2.6. Swelling potential and degradation potential of scaffolds

The swelling potential of the hydrogel scaffolds was measured in distilled water at room temperature. For this, the known amounts of the scaffolds were dipped into water and removed after a certain time. The excess water was removed from the surface of the scaffolds with tissue paper and measured the weight of the swollen scaffolds. After that, the scaffolds were again dipped in water, and this process was repeated several times. The swelling potential of the scaffolds was calculated using the following formula,

$$\%Swelling = \frac{W_s - W_d}{W_d} \times 100$$

$W_s$ and $W_d$ are the weight of swollen and dried scaffolds, respectively.

The degradation efficiency of the hydrogel scaffolds was analyzed with protease (1 mg/mL) enzyme at room temperature. For this, the calculated weight of the scaffolds was kept in enzyme media for a fixed time. After that, the scaffolds were removed from the media and rinsed with distilled water. The surface water was removed with the tissue paper, followed by the drying of the scaffolds. The weights of the dried scaffolds were taken, and this process was performed several times. The old enzyme media were replaced with fresh media after three days intervals. The degradation rate was calculated by using a given formula,

$$Weight\ Loss\ (\%) = \frac{W_i - W_d}{W_i} \times 100$$

$W_i$ and $W_d$ are the weight of initial and degraded scaffolds, respectively.

### 2.7. Conductivity and electrochemical analysis

The conductivity of the developed hydrogels was measured by using the four-probe instrument (MS Tech, Solution) connected with the Keithley 2460 source meter®. The electrochemical activity of the developed hydrogels was analyzed in the range of −0.6 *V*–1.2 V with the scan rate of 25 mV/s by the Keithley 2460 source meter®. The dimension of hydrogel used for electrochemical analysis was 2.2 × 0.8 × 0.4 $cm^3$.

### 2.8. Cell viability

The individual or co-cultured cell viability of HDF, HaCaT, and HUVEC was monitored by the WST-8 assay with the developed hydrogel scaffolds. For this, $1 \times 10^4$ (individual culture), and $0.3 \times 10^4$ (co-cultured) cells were incubated with or without the scaffolds for 1, 3, and 5 days in a 5% $CO_2$ incubator at 37 °C. The groups without the scaffolds treatment were to be considered as control. After incubation, WST-8 dye was added to the cultured media and incubated for 2 h to form formazan. The formazan quantities were measured with a spectrophotometer (Infinite® M Nano 200 Pro, TECAN, Switzerland) by taking absorbance at 450 nm. All experiments were accomplished in triplicate ($n = 3$), and the results are shown at mean ODs ± standard deviations (SD). Statistical significance was taken at $^*p < 0.05$.

### 2.9. Cell morphology

The morphologies of the individually and co-cultured cells were visualized by using an inverted fluorescence microscope (DMi8 Series, Leica Microsystems, Germany) after 3 days of treatment. For this, $2.0 \times 10^4$ (individual cells) and $0.5 \times 10^4$ (co-cultured cells) were incubated with or without scaffolds. The groups without any scaffolds treatment were taken as control. After that, cells were washed with PBS and fixed by 4% paraformaldehyde (PFA) (Sigma-Aldrich, USA) solution. The fixed cells were washed with PBS and treated with 0.1% Triton-X 100 for 10 min, followed by 1% bovine serum albumin (BSA) (Sigma-Aldrich, USA) treatment for 60 min. After that, cells were stained with 200 μL of Alexa Flor 488-conjugated Phalloidin (F Actin Probe; Invitrogen, Thermo-Fischer Scientific, USA) for 20 min, and followed by nuclei staining with 4, 6-diamino-2-phenylindole dihydrochloride (DAPI) (Sigma-Aldrich, USA) for 5 min. The excess stains were removed by washing with PBS, and mounting was performed by adding 1 drop of Prolong® Antifade mounting media (Invitrogen, Thermo-Fischer Scientific, USA), and images were captured with the microscope.

### 2.10. RNA extraction and real-time polymerase chain reaction (qPCR) analysis

The qPCR technique was utilized to examine the mRNA expression in HDF, HaCaT, and HUVEC with or without the scaffolds. The groups without any treatment were taken as control. For this, $1 \times 10^6$ cells were cultured with Dulbecco Modified Eagle Medium (DMEM) in a 24 well-plate for 7 and 14 days, followed by the RNA extraction using TRIzol® reagent as per manufacturer's guidelines. The spectrometer was used to monitor the purity and concentration of the extracted RNA, followed by cDNA synthesis using reverse transcriptase. The qPCR was performed with SYBR Green Master mix with the reaction conditions involved 43 cycles of denaturation for 15 s at 95 °C and 1 min amplification at 60 °C. All reactions were completed in triplicate ($n = 3$) and normalized with glyceraldehyde 3-phosphate dehydrogenase (GAPDH) housekeeping gene. The Bio-Rad Real-Time PCR (CFX96TM Maestro Real-Time System, BioRad, USA) system was utilized to measure the expression of mRNA. The relative mRNA expression levels in different skin cells with control and scaffolds treated groups were compared in a histogram. The primers used in this study are given in Table S1.

### 2.11. Immunocytochemical analysis of protein marker

The immunocytochemical analysis was performed to examine the different protein expressions, including fibronectin, basic cytokeratin, and platelet endothelial cell adhesion molecule-1 (PECAM-1)/cluster of differentiation 31 (CD 31) in HDF, HaCaT, and HUVEC, respectively. For this, $2 \times 10^4$ cells (individually) in 24 well plates and cultured for 14 days with or without the scaffolds. The groups without scaffolds treatment were considered as control. After that, cells were washed with PBS and fixed with 4% PFA solution for 20 min at room temperature. The 0.1% Triton X-100 solution was used to permeabilize the cells for 15 min at room temperature, washed with PBS, and blocked by 1% BSA reagent. Finally, cells were treated with 250 μL of mouse monoclonal antibodies against fibronectin, basic cytokeratin, and PECAM-1, followed by the nuclei counterstaining with 20 μL of DAPI solution for 2 min. The excess stain was removed by washing with PBS, and mounting was done by adding mounting media. The morphologies were captured with the fluorescence microscope.

### 2.12. Antibacterial potential of the hydrogel scaffolds

The antibacterial activity of the hydrogel scaffolds was analyzed using the colony counting method and measuring the optical density (OD) of the *Bacillus subtilis* (ATCC-6051), as earlier reported (Ma et al., 2020). For the colony counting method, 100 μL of the bacteria solution ($1 \times 10^6$) (Difco™, Nutrient broth, BD Biosciences, USA) was added to a petri dish containing 25 mL of the culture media with materials (20 mg/mL) and cultured for 24 h at 37 °C. The groups without hydrogels were considered as control. After that, 100 μL of the bacteria solution was transferred onto agar plates and further cultured for 24 h to form the colony.

The prepared scaffolds were incorporated into a bacterial medium ($1 \times 10^6$) for OD measurement and treated for 6, 24, and 48 h. The media without scaffolds served as control. The OD change was measured using a spectrophotometer at 600 nm. The tests were performed in triplicate.

### 2.13. In vivo wound healing analysis

The *in vivo* study was performed to monitor the wound healing efficiency of the developed hydrogel scaffolds with the three weeks old Institute of Cancer Research (ICR) male rats (total number of rats = 6) after 7 and 14 days of implantation. The experiment was divided into negative control-without treatment, positive control-pure polymer scaffolds (CMCS), and experiment group-CMCS/s-NC 1. Here, we chose the CMCS/s-NC 1, as an experimental group because of its better skin proliferation potential than other scaffolds *in vitro*. Each group has duplicate rats (number of rats = 2) with two experiment sites. In brief, the dorsal hairs of the rats were cleaned, and skin was disinfected with 70% ethanol solution. After that, a circular wound of 1 cm diameter was generated by using a sterile biopsy punch. The two layers of the dorsal skin were removed and filled with the scaffolds. All rats were placed in a protected and sound-proof room. The room temperature and relative humidity were maintained at 21 ± 1 °C, and 35 ± 1%, respectively. The room was maintained with an automatically controlled 12 h light and 12 h dark cycle. All possible efforts were made to minimize the animal suffering and number of animals required to produce consistent scientific results. After 14 days of treatment, the rats were sacrificed to perform the histological staining.

For histological analysis, the collected specimens were fixed with 3.7% PFA solution for 2 days, then decalcified with 12% ethylene diaminetetraacetic acid (EDTA) at 4 °C. After that, the specimens were cleaned and dehydrated with alcohol. The dehydrated specimens were implanted in paraffin to produce fine sections. The specimen sections

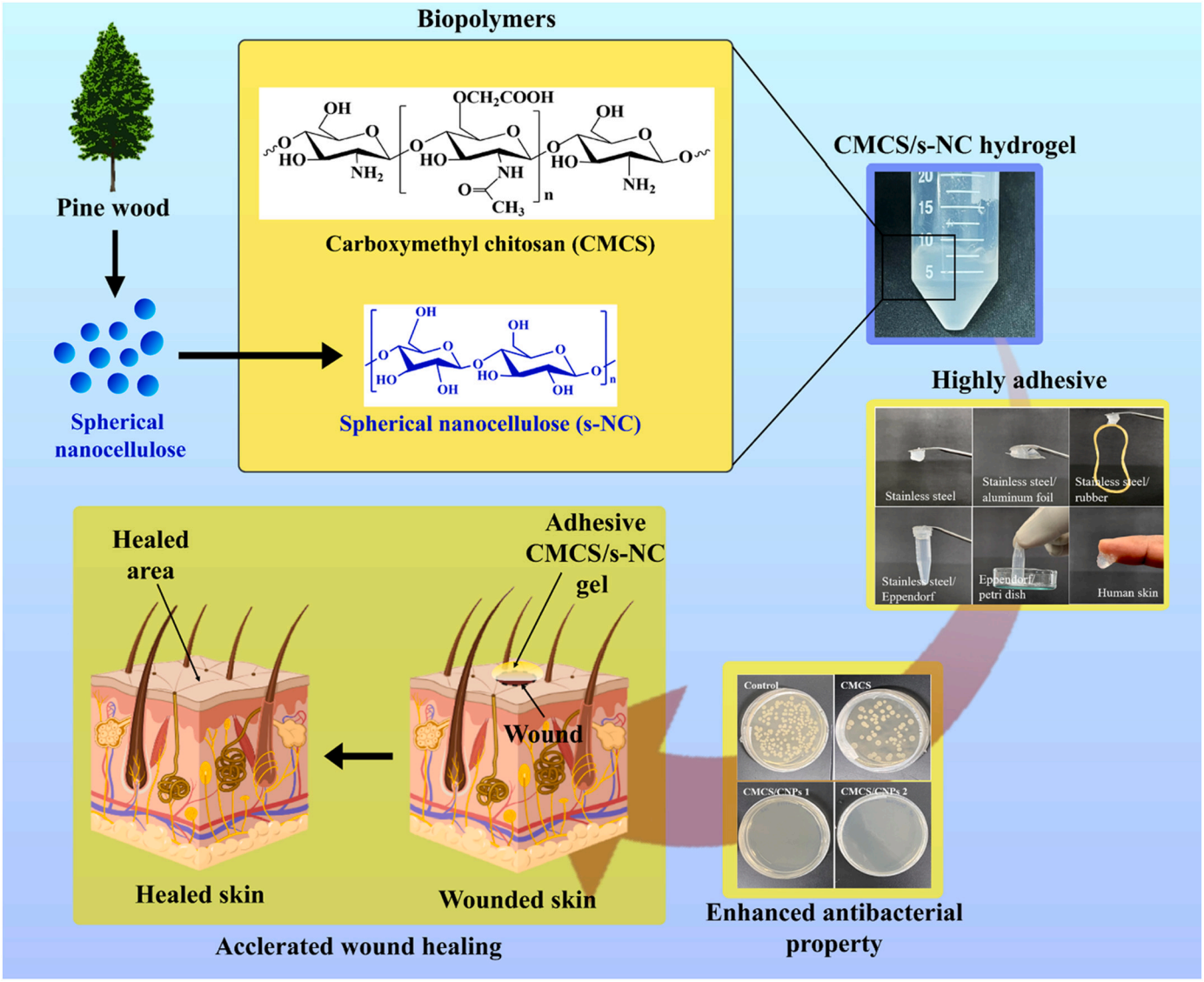


**Scheme 1.** The schematic demonstration for the preparation of the hydrogel and its potential application for cutaneous wound healing

were stained with hematoxylin (H), eosin (E), and Masson's trichrome (MT). All surgical protocols were approved by the Capital Medical University Animal Experimental Ethics Committee (AEEC, Institute of Animal Care and Use Committee of Capital Medical University, Permission No. KQYY-202012-004). The scaffolds were sterilized by UV light treatment before the implantation.

### 2.14. Statistical analysis

Statistical analyses were performed with one-way ANOVA using Origin Pro9.0 software. All results were presented as mean ± standard deviations (SD). Statistical significance was considered at $*p < 0.05$, $**p < 0.01$, and $***p < 0.001$. All comparisons were made between the control and treated groups.

## 3. Results and discussion

### 3.1. Characterizations of s-NC and CMCS

A schematic presentation for synthesizing the hydrogel scaffolds and their potential application in wound healing is shown in (Scheme 1).

The FTIR spectra of cellulose and s-NC are shown in (Fig. S1a). The characteristic peaks at 3325, 1640, and 1019 $cm^{-1}$ are attributed to the hydroxyl (–OH) group, absorbed water, and –C–O stretching groups, respectively. The cellulose and s-NC showed no significant peaks at 1500 $cm^{-1}$, suggesting the removal of the lignin moiety from their structures by chemical treatment. The appearance of the additional absorption peaks at 1731 $cm^{-1}$ in the s-NC is attributed to carboxylation of cellulose functional groups by APS reagent (Cheng et al., 2014). No other significant changes were observed in the s-NC spectrum, suggesting that APS hydrolysis did not alter the structural integrity of pure cellulose. The morphology of the obtained s-NC was examined by AFM, and the images are shown in (Fig. S1b). The obtained s-NC exhibited spherical morphology with an average diameter of ~60 nm, indicating the successful formation of nanoparticles by APS hydrolysis. The XRD patterns of the cellulose and s-NC are shown in (Fig. S1c). The diffraction peaks at 11.8°, 20.0°, and 21.5° were attributed to cellulose I and II structures (Patel et al., 2020). The s-NC exhibited sharper and more intense diffraction peaks than cellulose, indicating the enhanced crystallinity of the s-NC due to the removal of amorphous zones. The proton spectrum of the synthesized CMCS with the indicated peaks is given in (Fig. S2). The proton-NMR pattern is similar to previously reported literature. Therefore, we anticipated that the synthesized CMCS would be highly pure (Bukzem et al., 2016; Luo et al., 2018).

### 3.2. Interaction and morphological characterization of hydrogel scaffolds

The FTIR spectrum of pure CS is given in (Fig. S3a). The characteristic peaks of the CS polymer are indicated in the spectrum. The broad characteristic peak at 3324 $cm^{-1}$ in the pure CS can be attributed to the hydrogen-bonded amine ($-NH_2$) functional groups, which shifted toward lower wavenumbers (3324 → 3303 $cm^{-1}$) in the CMCS hydrogel. The FTIR spectra of CMCS and its indicated hydrogels in the absorption regions of 4000–2500 $cm^{-1}$ are given in (Fig. S3b). The broad

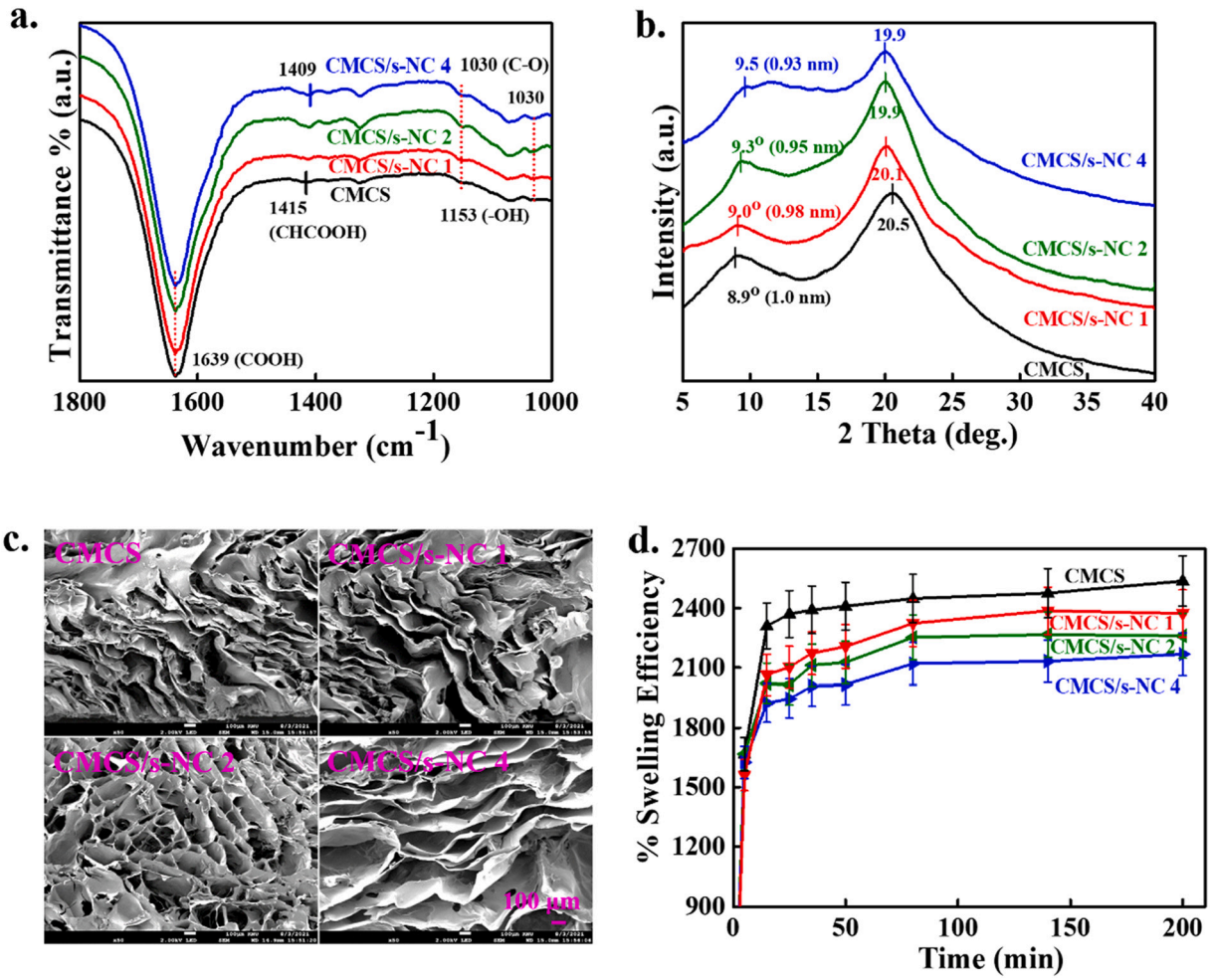


**Fig. 1.** The structural and morphological analysis of the developed hydrogel scaffolds. (a) FTIR spectra of the hydrogels, (b) XRD patterns of the hydrogel scaffolds, (c) SEM morphologies of the hydrogel scaffolds, and (d) Swelling potential of the developed hydrogel scaffolds ($n = 3$).

absorption peak at 3303 $cm^{-1}$ in the developed hydrogels is assigned for the hydrogen-bonded amine/hydroxyl functional groups (Doshi et al., 2017). The FTIR spectra of CMCS and its composite hydrogels in the absorption regions of 1800–1000 $cm^{-1}$ are shown in (Fig. 1a). The absorption peak at 1639 $cm^{-1}$ in CMCS is assigned to the carboxyl group, overlapping with the amino groups. The absorption peak at 1156 $cm^{-1}$ weakened in CMCS, indicating that carboxymethylation occurred at the hydroxyl groups of CS (Luo et al., 2018). The absorption peak in CMCS at 1415 $cm^{-1}$ is attributed to the symmetric stretching vibration of the $COO^-$ functional group. A shift in the absorption peak (1415 → 1409 $cm^{-1}$) was observed in the composite hydrogels, suggesting the physical interaction between the functional groups of incorporated s-NC and CMCS polymer matrix. This shift in the composite hydrogels can be attributed to the depreciation of the intramolecular hydrogen bonding between the polymer chains and increased intermolecular hydrogen bonding between the incorporated s-NC and polymer chains (Patel et al., 2021). This result suggests that hydrogen bonding is vital for such changes in the developed hydrogels.

The structural changes in the developed hydrogels were evaluated using an X-ray diffractometer, and the XRD patterns are shown in (Fig. 1b). The broad and sharp diffraction peaks at 8.9° and 20.5° were observed in the CMCS, demonstrating the amorphous and crystalline zones in the structure, respectively. A similar XRD pattern of water-soluble CMCS has been earlier shown in the literature. (Baran et al., 2015; Bukzem et al., 2016). The composite hydrogels exhibited diffraction patterns similar to those of the pure polymer, with slight changes in the peak position. A decrease in the interplanar distance of the amorphous zones (1 → 0.93 nm) was observed in the composite hydrogels, indicating the formation of the minor assembled structure due to the interaction between the incorporated s-NC and polymer chains as observed in the FTIR results. No significant changes in the crystalline interplanar distance were observed in the composite hydrogels (0.44 → 0.45 nm), suggesting that the distributions of s-NC have predominantly occurred in the amorphous zones of the polymer.

The surface morphologies of the hydrogel scaffolds were analyzed using SEM, and the images are shown in (Fig. 1c). The fabricated scaffolds exhibited a highly porous and interconnected morphological structure. Layered structures were observed in the scaffolds. The composite scaffolds demonstrated a more porous morphology than the pure polymer scaffold.

The swelling efficiency of the scaffold plays a vital role in tissue engineering applications as it facilitates the exchange of cell metabolites and nutrients (Tao et al., 2017). The swelling potential of the developed hydrogel scaffolds was examined under aqueous conditions at room temperature, and the results are shown in (Fig. 1d). The composite hydrogel scaffolds showed a lower swelling efficiency than pure polymer scaffolds, and this potential further decreased with increasing s-NC content. The decrease in the swelling efficiency might be due to the unavailability of free hydrophilic hydroxyl (–OH) or amine ($–NH_2$) groups in the composite scaffolds in the presence of s-NC. The addition of the s-NC in the polymer matrix might lead to a physically cross-linked structure, decreasing swelling efficiency. A similar result was earlier reported in cellulose nanocrystals incorporated carboxymethyl chitosan scaffolds (Zhang et al., 2019). The swelling of the scaffolds should be controlled under physiological conditions, and rapid swelling may weaken and degrade the scaffolds. Furthermore, no enhancement in the swelling efficiency was observed after 15 h, indicating the saturation point of the fabricated hydrogel scaffolds.

An *in vitro* degradation study was performed to monitor the degradation rate of the developed hydrogel scaffolds, and the results are presented in (Fig. S4). The composite scaffolds exhibited a greater degradation rate than the pure polymer scaffolds in the presence of protease. The higher degradation rate might be attributed to the structural damage of the physically cross-linked composite scaffolds and leaching out of the filled s-NC, which accelerated the degradation process. The leaching of s-NC from the composite scaffolds facilitated the insertion of the protease enzyme within the polymer matrix, causing a greater degradation. Our finding is consistent with the previously reported results, where an enhanced degradation of cellulose nanocrystal added carboxymethyl chitosan scaffolds occurred with a lower swelling efficiency (Zhang et al., 2019). The scaffolds should have an appropriate rate of degradation for tissue-engineering applications.

### 3.3. Rheological and recovery strength of hydrogels

For tissue engineering applications, the developed hydrogel should have good elasticity and mechanical strength. The rheological properties of the prepared hydrogels were analyzed using a rheometer, and the results are presented in (Fig. 2). The change in the storage modulus (G′, with lines) and loss modulus (G″, no lines) in the measured frequency regions are given in (Fig. 2a). The composite hydrogels exhibited higher G′ values than the pure polymer hydrogel, showing high elasticity owing to the greater interaction between s-NC and polymer chains. Significant enhancement in the G′ values ($1.11 \times 10^5$ Pa → $5.64 \times 10^6$ Pa) was observed in the composite hydrogels due to the greater interaction between polymer chains and s-NC, creating the interconnected network structure, leading to high elasticity. The enhancement in the G′ values at high ω regions in the composite hydrogels can be explained by the relaxation and formation of more interconnected network structures, resulting in a solid-like structure and higher G′ values (Pati et al., 2014; Yang et al., 2013). The higher G″ values were observed in the composite hydrogels than the pure polymer hydrogel, and its value further increased with increasing s-NC content. However, the magnitude of G″ was lower than G′ throughout the measured ω regions, suggesting the formation of stable elastic polymeric network structures in the hydrogels.

The change in the complex viscosity (η*) of the developed hydrogels in the ω region was also measured, and the results are shown in (Fig. 2b). A higher η* value was observed in the composite hydrogels than in the pure polymer hydrogels in the measured regions, further increasing with increasing s-NC content, indicating more solid-like properties in the composite hydrogels. The enhanced η* value was observed in the lower ω regions, whereas a decrease in the η* value occurred at higher ω regions, suggesting shear thickening and shear thinning properties, respectively. These are the anticipated properties of printing applications.

The thixotropic behavior of the developed hydrogels was analyzed to confirm their recoverable potential after applying a high shear rate. For this, a series of shear rates of 0.1, 1000, and 0.1 $s^{-1}$ (each for 100 s) was applied to monitor the change in the η* value of the hydrogels. We used a high shear rate (1000 $s^{-1}$) to deform the structure. Recoverable hydrogels have received wide attention in printing and tissue engineering applications (Abouzeid et al., 2018). They can easily re-gained their original physicochemical properties after the deformation (Han et al., 2017). The changes in the η* value at different shear rates are shown in (Fig. 2c). The initial η* values of CMCS, CMCS/s-NC 1, CMCS/s-NC 2, and CMCS/s-NC 4 were 1314, 4335, 695, and 562 Pa, which decreased to 0.552, 0.326, 0.443, and 0.687 Pa at a high shear rate (1000 $s^{-1}$), respectively. This value was further increased at low shear rates (0.1 $s^{-1}$), and were 681, 2787, 484, and 475 Pa for CMCS, CMCS/s-NC 1, CMCS/s-NC 2, and CMCS/s-NC 4, respectively. The recovery potential was 51.7, 64.2, 69.2, and 84.2% for CMCS, CMCS/s-NC 1, CMCS/s-NC 2, and CMCS/s-NC 4. The high recovery potential of the composite hydrogels is attributed to the formation of interconnected polymeric network structures with incorporated s-NC, which restricted the deformation of the hydrogels.

The injectability potential of the developed hydrogels was tested using a syringe at room temperature, and a digital image of the injected hydrogel is shown in (Fig. 2d). The hydrogel was easily injected and retained its structure. Injectable hydrogels have diverse advantages and can be injected at the desired sites (Zhang et al., 2014). Injectable hydrogels are considered appealing materials for skin wound

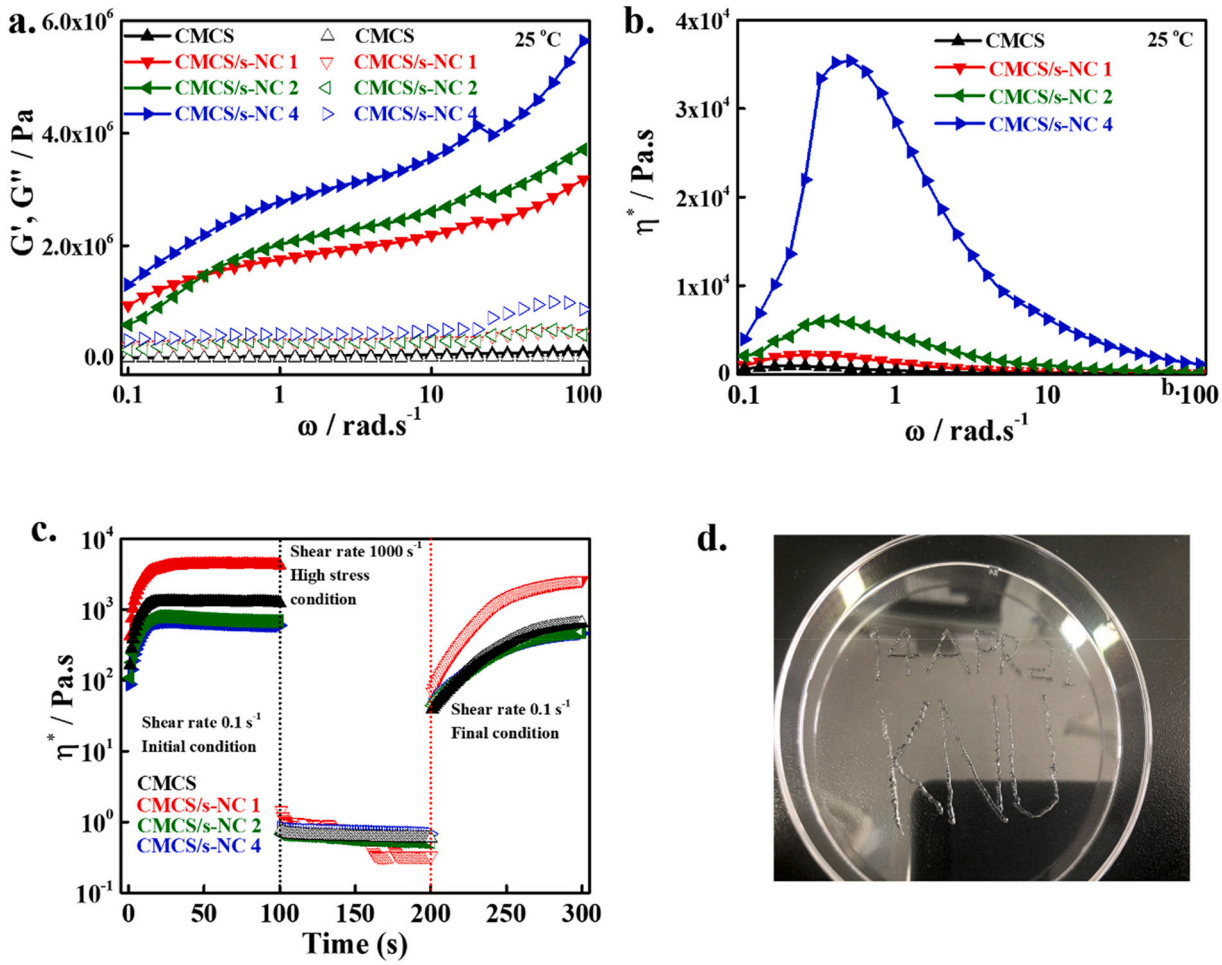


**Fig. 2.** Evaluation of the rheological strength of the developed hydrogel at 25 °C. (a) Storage and loss moduli of the hydrogels, (b) Corresponding viscosity complex of the hydrogels, (c) Analysis of thixotropic behavior of the developed hydrogel at 25 °C, and (d) Image of the injected hydrogel in the desired patterns.

regeneration because they reduce gel fragmentation potential at the implanted sites even after external mechanical deformation and can persistently facilitate skin wound curing (Chen et al., 2019). They can also be applied to irregular wound sites.

### 3.4. Adhesive potential of hydrogels

The adhesive properties of the developed hydrogel were examined with different surfaces, and the images are shown in (Fig. 3a). The developed hydrogel promptly adhered to different surfaces, showing its adhesive potential. The adhesiveness of the developed hydrogels can be attributed to multiple interactions (covalent and noncovalent) between the functional groups of the hydrogels and the material surface (Bovone et al., 2021). Adhesiveness is highly desirable for various applications, including stopping bleeding, sealing leakage, binding tissues, and improving tissue recovery (Nie et al., 2013). A schematic representation of the lap shear test is presented in (Fig. 3b). The developed hydrogels were sandwiched between two pieces of a plastic substrate (25 mm × 15 mm) and measured. The obtained curves of the adhesive strength *versus* displacement for different hydrogels with plastic are shown in (Fig. 3c). An enhancement in the adhesiveness was observed in the composite hydrogels compared to the pure polymer hydrogel, indicating its adhesive potential. This potential was further enhanced by increasing the s-NC content in the polymer matrix, indicating its improved adhesive properties. The enhanced adhesiveness was due to strong interactions between the surfaces. Different factors, including adhesion time, properties of the hydrogels, and applied substrates, have widely influenced adhesiveness (Cui et al., 2019; Qu et al., 2018). The quantitative values of the adhesive strength of the developed hydrogels with plastic substrates are presented in (Fig. 3d). The adhesive strength was 5.53, 11.84, 15.13, and 18.32 kPa for CMCS, CMCS/s-NC 1, CMCS/s-NC 2, and CMCS/s-NC 4, respectively. It is anticipated that the adhesiveness potential of the developed hydrogels could be further increased with the hydrophilic surfaces, including pig and human skin, owing to the strong interaction between the polar groups of the tissue surface and the hydrogel, and can be applied for skin wound healing (Pei et al., 2020).

The possible mechanism for the adhesiveness of the developed hydrogel with different substrates is presented in (Fig. 3e). Herein, we illustrate the interaction mechanism between the glass and human skin surfaces by the hydrogel surface. The hydrogels have charged ions ($NH_4^+$ and $COO^-$), which can interact with other polar or charged functional groups of the materials *via* dipole-dipole or ion-dipole interactions, causing the hydrogel to be challenging to remove from the surfaces. Glass has negatively charged silicate groups and interacts with positively charged amino groups of the hydrogel through the interaction mentioned above. Similarly, the skin surface can interact with the hydrogel.

### 3.5. Conductivity and electrochemical analysis of hydrogels

The conductive property of the developed hydrogels was measured by the four-probe technique, and the results are presented in Table 1. A significant enhancement ($6.815 \times 10^{-5} \rightarrow 2.892 \times 10^{-3}$ S/cm) in the conductivity was observed in the composite hydrogels compared to the

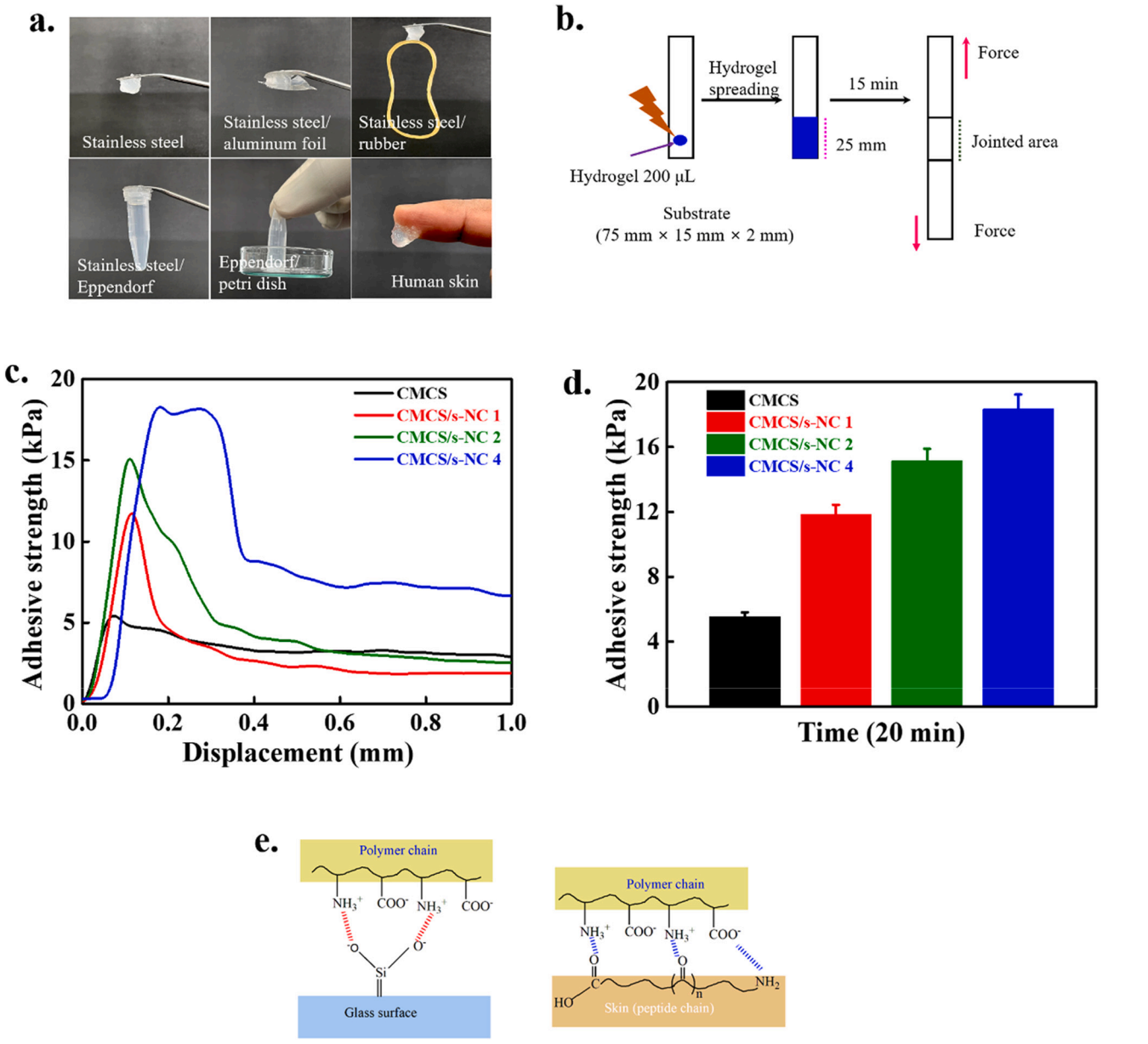


**Fig. 3.** (a) Examination of the adhesiveness of the developed hydrogels with different surface, (b) Schematic demonstration of the adhesion strength measurement, (c) Adhesion shear force *versus* displacement of the hydrogels with plastic, (d) Adhesive strength of the hydrogels with plastic substrate ($n = 3$), and (e) The possible interactions of the hydrogels with different surfaces.

**Table 1**
Analysis of the conductivity of the developed hydrogels using the four-probe system.

| Sample | Dimension (cm) | Resistance (R) (ohm) | Conductivity = L/RA (S/cm-1) |
|---|---|---|---|
| CMCS | 2.4 × 0.9 × 0.5 | 1629.73 | $6.817 \times 10^{-5}$ |
| CMCS/s-NC 1 | 2.3 × 1.0 × 0.3 | 1599.61 | $6.251 \times 10^{-4}$ |
| CMCS/s-NC 2 | 2.4 × 0.9 × 0.6 | 1572.22 | $7.067 \times 10^{-4}$ |
| CMCS/s-NC 4 | 2.2 × 0.6 × 0.4 | 864.39 | $2.892 \times 10^{-3}$ |

pure polymer hydrogel. This enhancement in the conductivity is attributed to the more protonation of the amino-functional groups of CMCS in the presence of s-NC, which facilitated the improved ionic conductivity. The developed hydrogels exhibit ionic conductivity within the range of skin conductivity (2.6–1 × $10^{-4}$ mS/cm) (Korupalli et al., 2020). Thus, it is anticipated that the developed hydrogels, which have excellent adhesive properties with conductivity, can significantly stimulate the skin cell activities after implantation and assist the rapid wound healing process. Functionalization of chitosan not only improves its water solubility but also enhances its ionic conductivity (Wan et al., 2003).

The cyclic voltammetry was conducted to assess the electrochemical behavior of the developed hydrogels using a three-electrode system, and the results are shown in (Fig. 4). The pure polymer hydrogel exhibits oxidation and reduction peaks at 0.41 V and − 0.015 V, indicating the protonation and deprotonation of the –NH and –COOH functional groups of CMCS polymer, respectively (Wu & Zhu, 2018). A systematic shift in the oxidation (0.41 → 0.77 V) and reduction (−0.015 → 0.051 V) peaks was observed in the composite hydrogels, suggesting that the addition of s-NC in the polymer matrix facilitates the electrochemical activity of the hydrogels. The composite hydrogels exhibit a greater

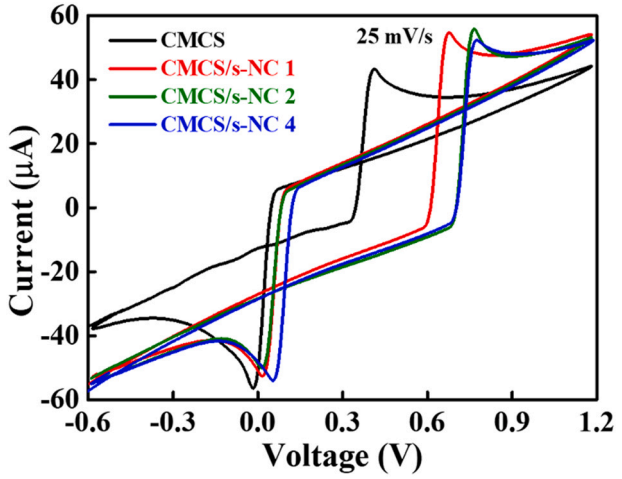


**Fig. 4.** Electrochemical analysis of the developed hydrogel at 25 mV/s scan rate.

anodic current (0.41 → 0.76 μA) compared to the pure polymer hydrogel, showing their improved electrochemical performances in the presence of s-NC. The enhanced electrochemical performances of the composite hydrogels can be attributed to the bridging effects of s-NC functional groups (–COOH, and –OH), which facilitated the electron transfer. Additionally, a pronounced box-like hysteresis was observed in the developed hydrogel, suggesting the electro-oxidation of the hydrogel at the electrode surface (Chia et al., 2019). The hysteresis area was further increased in the composite hydrogels, demonstrating the greater electro-oxidation of the hydrogels at the electrode surface.

### 3.6. Biocompatibility and cell morphology

Before evaluation of the biocompatibility of the developed hydrogel scaffolds, we assessed the cellular activity of the CNCs and s-NC through WST-8 assay at different periods (1, 3, and 5 days), and results are given in (Fig. S5). The media without nanocellulose were considered to be controlled. We chose 1% nanocellulose content to examine their cellular response. 1% nanocellulose exhibited greater cellular activity (Patel et al., 2019b). The nanocellulose treated groups demonstrated enhanced cell viability than control, showing their enhanced biocompatibility. Interestingly, s-NC treated media have higher cell viability than CNCs treated groups. The enhanced cell viability is attributed to the higher surface area of s-NC than CNCs, which facilitated cellular activity.

The biocompatibility of the fabricated hydrogel scaffolds was assessed using skin cells (HDF, HaCaT, and HUVEC) using the WST-8 assay, and the results are shown in (Fig. 5). We performed individual cell culture in the presence of the hydrogel scaffolds, followed by co-culture to examine the effects of the developed hydrogel scaffolds on skin cells. The HDF viability in the presence of the hydrogel scaffolds after 1, 3, and 5 days of treatment is shown in (Fig. 5a). The groups without treatment were considered the control group. No adverse effects were observed in the presence of the hydrogel scaffolds, indicating their biocompatibility. The composite scaffolds demonstrated greater cell viability than the control scaffolds. The groups containing CMCS/s-NC 1 hydrogel scaffolds exhibited enhanced viability compared to the other scaffolds, indicating improved biocompatibility. Fibroblasts play an essential role in skin physiology and cutaneous wound healing. It produces all ECM components, such as adhesive and structural proteins, proteoglycans, and glycosaminoglycans (Kendall & Feghali-Bostwick, 2014). The cytotoxicity of the hydrogel scaffolds was analyzed using the HaCaT cells, and the results are shown in (Fig. 5b). Media without scaffold treatment were used as controls. The hydrogel scaffolds had no toxic effects on HaCaT cells, indicating their biocompatibility. The composite scaffolds exhibited higher cell viability than the pure polymer scaffolds and the control. The improved biocompatibility of the composite scaffolds was attributed to their open morphological structure and bioactivity potential. HaCaT cells act as a barrier for foreign substances and reduce moisture and heat loss from the body (Hunt et al., 2009). The biocompatibility of the hydrogel scaffolds was also monitored with HUVECs after different time intervals, and the results are shown in (Fig. 5c). The groups without treatment were considered as the controls. No cytotoxicity was observed in the scaffold-treated groups, indicating its biocompatibility. Higher cell viability was observed with composite scaffolds than pure polymer scaffolds and control scaffolds, suggesting improved biocompatibility. HUVECs play a vital role in angiogenesis and vascularization. Newly generated tissues require an active blood vessel network for survival (Bok et al., 2018).

Furthermore, we co-cultured HDF, HaCaT, and HUVEC with the developed scaffolds to create a skin regeneration model, and the results are presented in (Fig. 5d). It was interesting to see that the developed scaffolds facilitated skin cell proliferation in all treated groups except CMCS/s-NC 4. The enhanced viability was observed with composite scaffolds compared to the pure polymer scaffolds, and this was more significant in CMCS/s-NC 1 treated media, indicating that 1% s-NC content is optimum for improved cellular activity. The enhanced cellular activity of the developed hydrogel scaffolds is due to their favorable topographical structure, adhesiveness, and improved bioactivity. The skin cells (containing peptide layer) strongly interacted with the surface of the scaffolds, and the open structure facilitated gaseous and nutrient exchange. However, a decrease in skin cell viability occurred in CMCS/s-NC 4 treated groups compared to the other treatments. This may be due to the higher concentrations of nanoparticles, their properties, and their shapes. Pereira et al. have previously reported the cytotoxicity of cellulose nanofibers (CNFs) toward mammalian cells at higher concentrations (Pereira et al., 2013). This result indicates that the developed scaffolds can accelerate skin cell regeneration.

The morphologies of the co-cultured cells were examined using a fluorescence microscope after 3 days of treatment, and the images are shown in (Fig. 5e). We chose the CMCS/s-NC 1 scaffold for the treatment groups because of its better cellular and bioactivity potentials. Media without scaffolds were used as controls. The cells were healthy and spread over the scaffolds. The cell densities were higher in the scaffold-treated groups than in control, confirming its superior biocompatibility, as observed in cell viability. The morphology of the individual cells (HDF, HaCaT, and HUVEC) after 3 days of treatment is shown in (Fig. S6). The cultured cells were healthy and elongated, except for the HaCaT cells. We also examined the only HDF proliferation behavior after 1, 3, and 5 days of treatment as proof for improved cellular activity, and the images are given in (Fig. S7). Cells were healthy on the scaffolds treated groups compared to control, showing improved biocompatibility.

### 3.7. Expression of mRNA and protein markers

The expression of HDF-associated gene markers (fibronectin and collagen 1A) in HDF was evaluated by the q-PCR technique after 7- and 14 days of treatment, and the results are shown in (Fig. 6a). The groups without scaffolds treatment were taken to be controlled. We selected the CMCS/s-NC1 composite scaffold to examine the gene expression potential than other composite scaffolds (CMCS/s-NC 2 and CMCS/s-NC 4) due to their improved cellular activity. A higher expression of fibronectin and collagen 1A was observed in the scaffolds treated groups than the control after 7 days of treatment which further increased after 14 days of incubation, showing their accelerating effects on HDF-associated gene markers. This was higher in CMCS/s-NC 1 scaffolds compared to the pure polymer scaffolds. The better expression of HDF-associated gene markers in CMCS/s-NC 1 is attributed to its better cellular activity and favorable topographical structures. Fibronectin is considered a crucial constituent of the ECM and is required for cell adhesion with stroma. It plays an important role in cytoskeleton modifications, cell migration, and differentiation. It also accelerates embryogenesis and

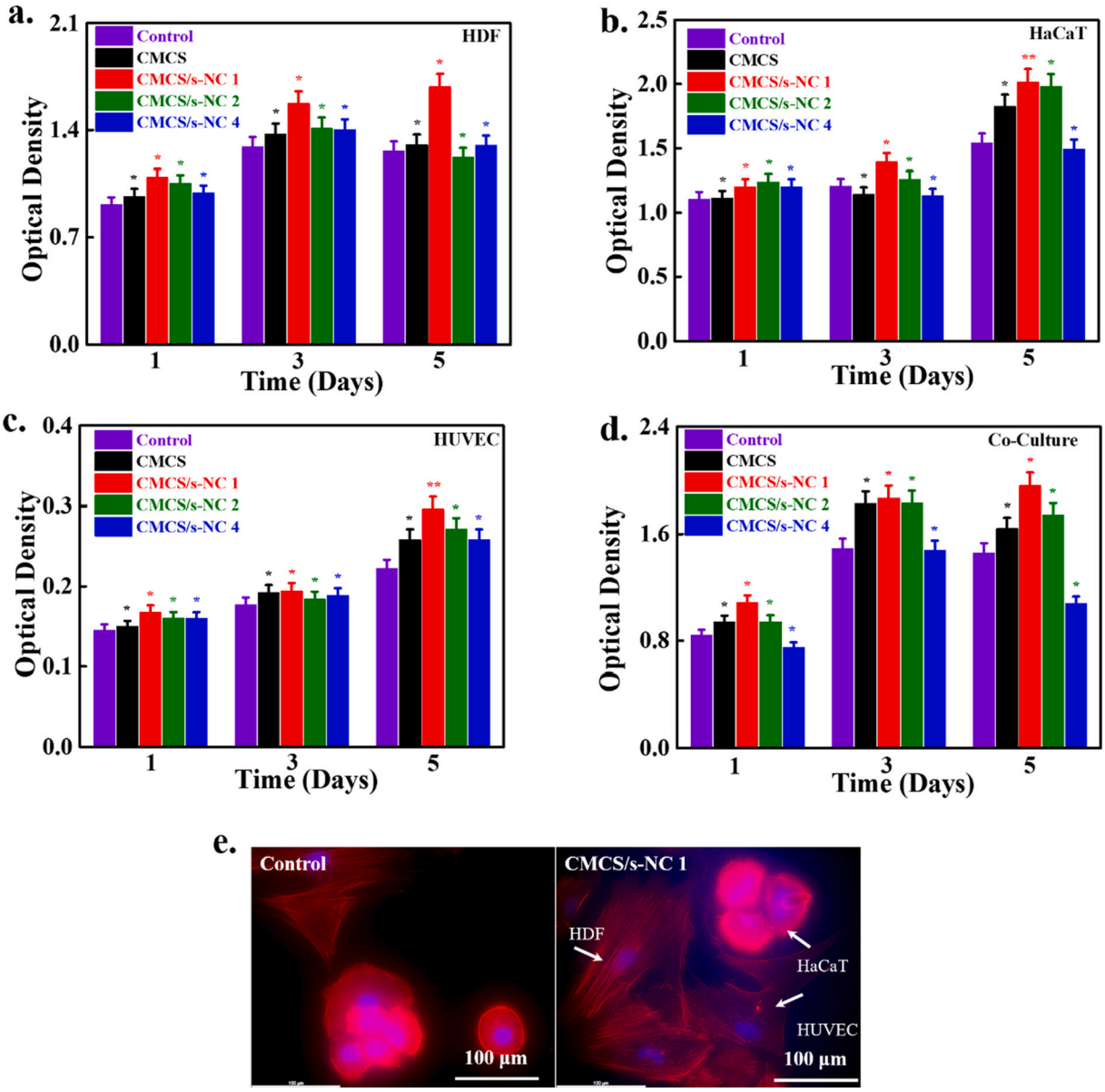


**Fig. 5.** Evaluation of the skin cell proliferation potential of the developed hydrogel scaffolds. Viability of (a) HDF, (b) HaCaT, (c) HUVEC, (d) co-cultured cells, and (e) Fluorescence morphologies of the co-cultured cells. The statistical analysis was performed between the control and treated groups ($n = 3$, $^{*}p < 0.05$, and $^{**}p < 0.01$). (Scale bar = 100 µm).

wound healing (Malakpour-Permlid et al., 2021). Collagen is the major fibrous glycoproteins in the ECM and facilitates ECM assembly, ECM-cell interactions, cell migration, and differentiation. The expression of different keratinocytes-related gene markers (KRT1, KRT5, KRT10, and KRT15) in HaCaT was also examined, and the results are given in (Fig. 6b). The media without scaffolds treatment are taken as control. A higher expression of keratinocytes-related gene markers occurred with scaffolds compared to the control, showing its keratinocytes generation efficiency. KRT1/10 are considered early gene markers whose expression was higher after 7 days of treatment and decreased after 14 days of incubation. KRT5/KRT15 are the important keratinocytes gene markers, and their expression occurs at the late stage of differentiation (Lima Cunha et al., 2021). The better expression of keratinocytes-related gene makers showed that the developed scaffolds could accelerate the keratinocytes formation, which plays an important role in wound repairing (Piipponen et al., 2020). We further examined the HUVEC-associated gene markers (vascular endothelial growth factor (VEGF); vascular endothelial-cadherin (VE-cadherin); and CD31) after 7, and 14 days of treatment, and the results are presented in (Fig. 6c). The groups without scaffolds were considered as control. A greater expression of HUVEC-related gene markers occurred with the scaffolds treated groups than the control, suggesting the angiogenic potential of the scaffolds, which further enhanced after 14 days of incubation. The CMCS/s-NC 1 treated groups' demonstrated enhanced expression than CMCS scaffolds due to their improved cellular activity. The VEGF, VE-CAD, and CD31 play significant roles in angiogenesis, maintenance, and organization of vascular structures (Dalle Carbonare et al., 2019). This result indicates that the developed scaffolds have efficiency and can promote angiogenesis.

We further examined the expression of fibronectin, basic cytokeratin, and PECAM-1 proteins in HDF, HaCaT, and HUVEC by using a fluorescence microscope after 14 days of incubation, and the results are presented in (Fig. 6d). The groups without any treatment were to be considered as control. The scaffolds treated groups expressed greater intensities of the above proteins than the control, suggesting that the developed scaffolds positively triggered the skin cell functions. The

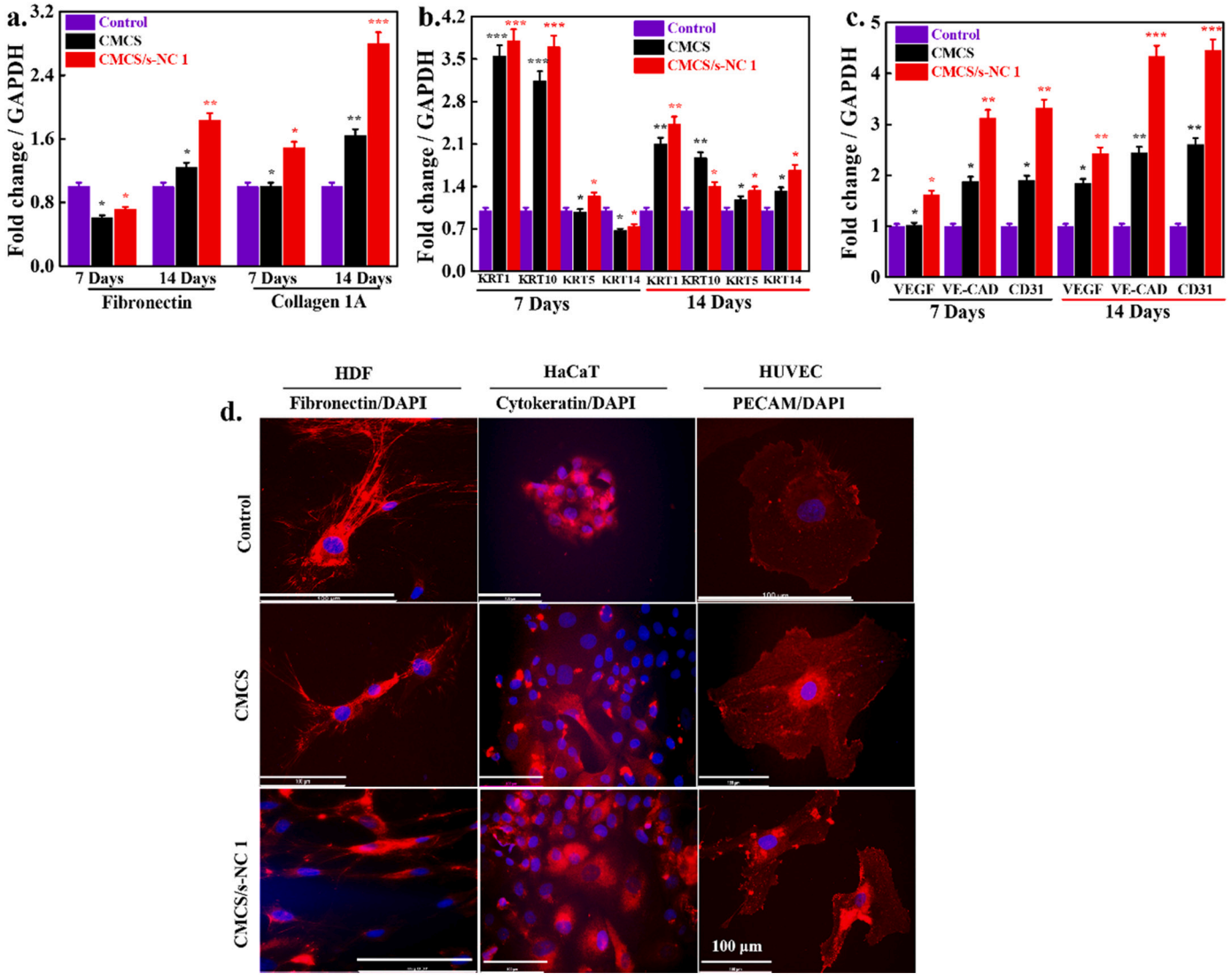


**Fig. 6.** Evaluation of the expression of skin-related gene markers, (a) HDF, (b) HaCaT, (c) HUVEC gene markers, and (d) Immunofluorescence images of the fibronectin, basic cytokeratin, and PECAM in HDF, HaCaT, and HUVEC, respectively. The statistical analysis was performed between the control and treated groups ($n = 3$, $*p < 0.05$, $**p < 0.01$, and $***p < 0.001$). (Scale bar = 100 µm).

expression of fibronectin protein occurred throughout the cytoskeleton of the HDF, whereas cytokeratin and PECAM-1 are more expressed in the vicinity of nuclei.

### 3.8. Antibacterial potential of hydrogels

The antibacterial potential of the developed hydrogels was examined using the colony counting method with *Bacillus subtilis* after 24 h of treatment, and the images are shown in (Fig. 7a). The groups without hydrogel treatment were used as controls. A significant reduction in the bacterial colony was observed in the hydrogel-treated groups compared to the control, indicating its antibacterial potential, and no colonies were observed in the composite hydrogel-treated plates, indicating their improved antibacterial potential. The antibacterial potential of the developed hydrogel is attributed to the presence of positively charged functional groups, which electrostatically interact with the bacterial cell membrane and damage it (Zhang et al., 2020). The improved antibacterial potential of the composite hydrogels may be attributed to the wrapping of the charged polymer chains with s-NC and more exposure to the bacteria, leading to more significant electrostatic interactions and consequently bacterial death. The antibacterial potential of the synthesized s-NC was also examined by the colony counting method with *Bacillus subtilis* after 24 h of treatment, and the images are shown in (Fig. S8). A slight decrease in the bacteria colony occurred with s-NC than control, suggesting that s-NC has no significant antibacterial potential.

We further measured the optical density of the cultured bacterial solution at different time intervals, and the results are shown in (Fig. 7b). The groups without treatment were considered as the controls. A significant decrease in the OD value was observed in the hydrogel-treated groups compared to the control after 6 h of treatment, showing their antibacterial potential, which further decreased with culture time (24 and 48 h), suggesting the improved antibacterial potential of the hydrogel. The composite hydrogels have a substantially lower OD value than the pure polymer hydrogel, indicating the enhanced antibacterial potential, which is consistent with the results of the colony counting method.

### 3.9. In vivo wound healing analysis

Wound healing is a complex biological process that involves different steps, including hemostasis, inflammation, migration, proliferation, and

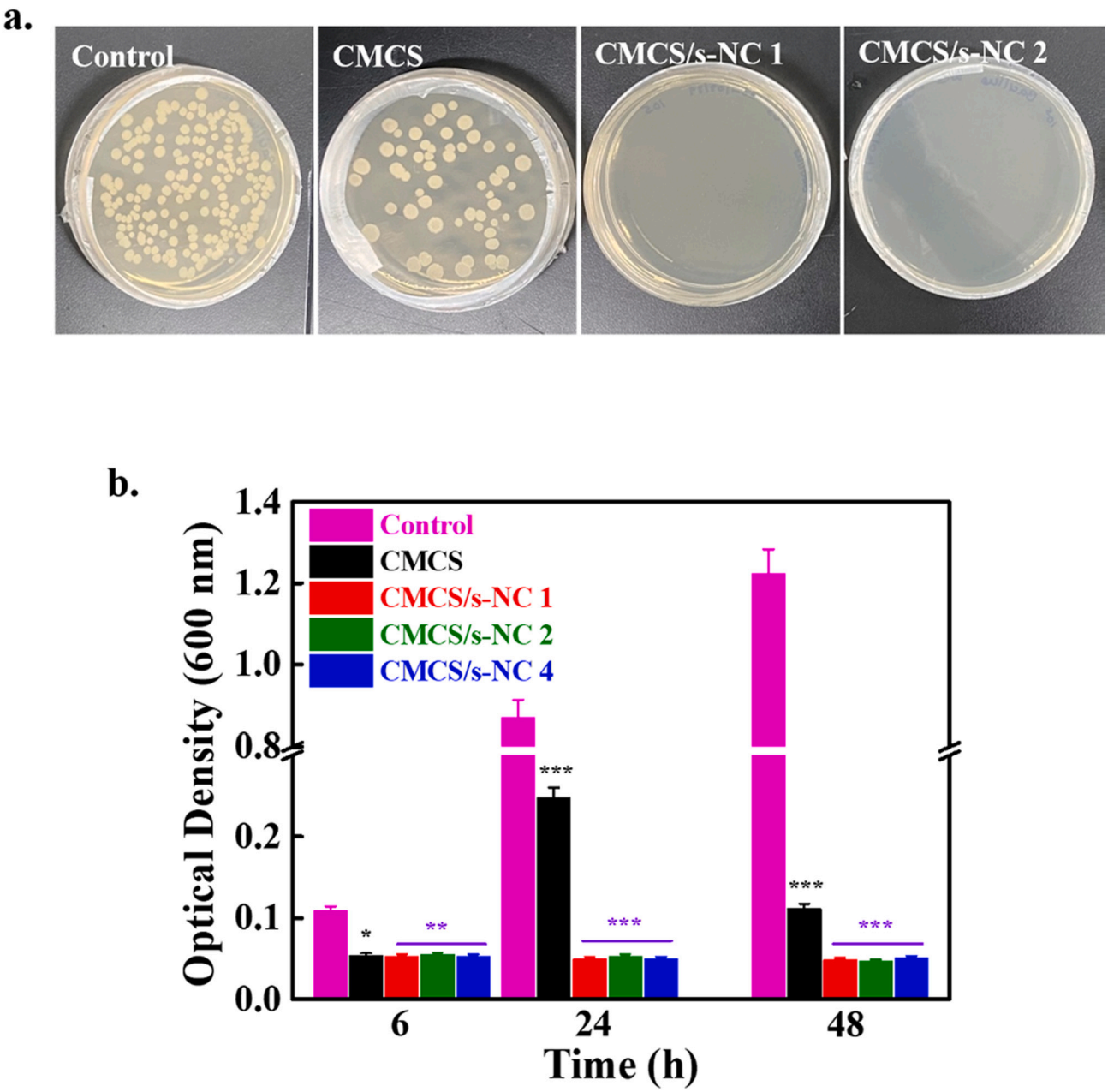


**Fig. 7.** Evaluation of the antibacterial potential of the developed hydrogels. (a) Colony counting method after 24 h of treatment, and (b) Optical density measurement method at different time intervals. The statistical analysis was performed between the control and treated groups ($n = 3$, $^{*}p < 0.05$, $^{**}p < 0.01$, and $^{***}p < 0.001$).

remodeling. We evaluated the subcutaneous wound healing potential of the developed hydrogel scaffolds using ICR rats based on *in vitro* analysis. A representative image of the used rats with the desired area for the implantation is shown in (Fig. 8a). We create the 1 cm spherical area for the wound healing process. A representative image of the wounded area with the implanted scaffolds is shown in (Fig. 8b). We used the two rats with two wound sites in each group to minimize the effects of other factors such as physiological changes and the number of experimental animals. The images of the used rats after 7 and 14 days of treatment are given in (Fig. 8c). The hydrogel scaffolds implanted groups' exhibit more wound closing potential than the control after 7 days of the treatment, which further enhanced after 14 days of treatment, demonstrating their wound healing efficacy. Among them, CSCM/s-NC 1 hydrogel scaffolds treated rats exhibited greater wound closing potential compared to the others. The improved skin regeneration efficacy of CSCM/s-NC 1 hydrogel scaffolds is attributed to their better cellular activity, which facilitated the skin cell proliferation and enhanced gene and protein expression, as observed in *in vitro* results. The quantitative results of the remaining wound area after 7 and 14 days of treatment are presented in (Fig. 8d). The results indicate that CSCM/s-NC 1 hydrogel scaffolds have better wound closing efficacy than others. The remaining wound area was $0.05 \pm 0.003$, $0.03 \pm 0.001$, and $0.02 \pm 0.001$ $mm^2$ for control, CMCS, and CMCS/s-NC 1 scaffolds after 14 days of implantation, respectively. Nearly complete wound healing was observed with the CSCM/s-NC 1 hydrogel scaffolds after 14 days of implantation, and the wound surface was covered with a newly generated epidermis.

H&E analysis was performed to examine the newly regenerated tissue with or without the scaffolds after 14 days of treatment, and the results are shown in (Fig. 8e). The formation of skin layers with blood vessels and hair follicles occurred in all groups; however, their densities

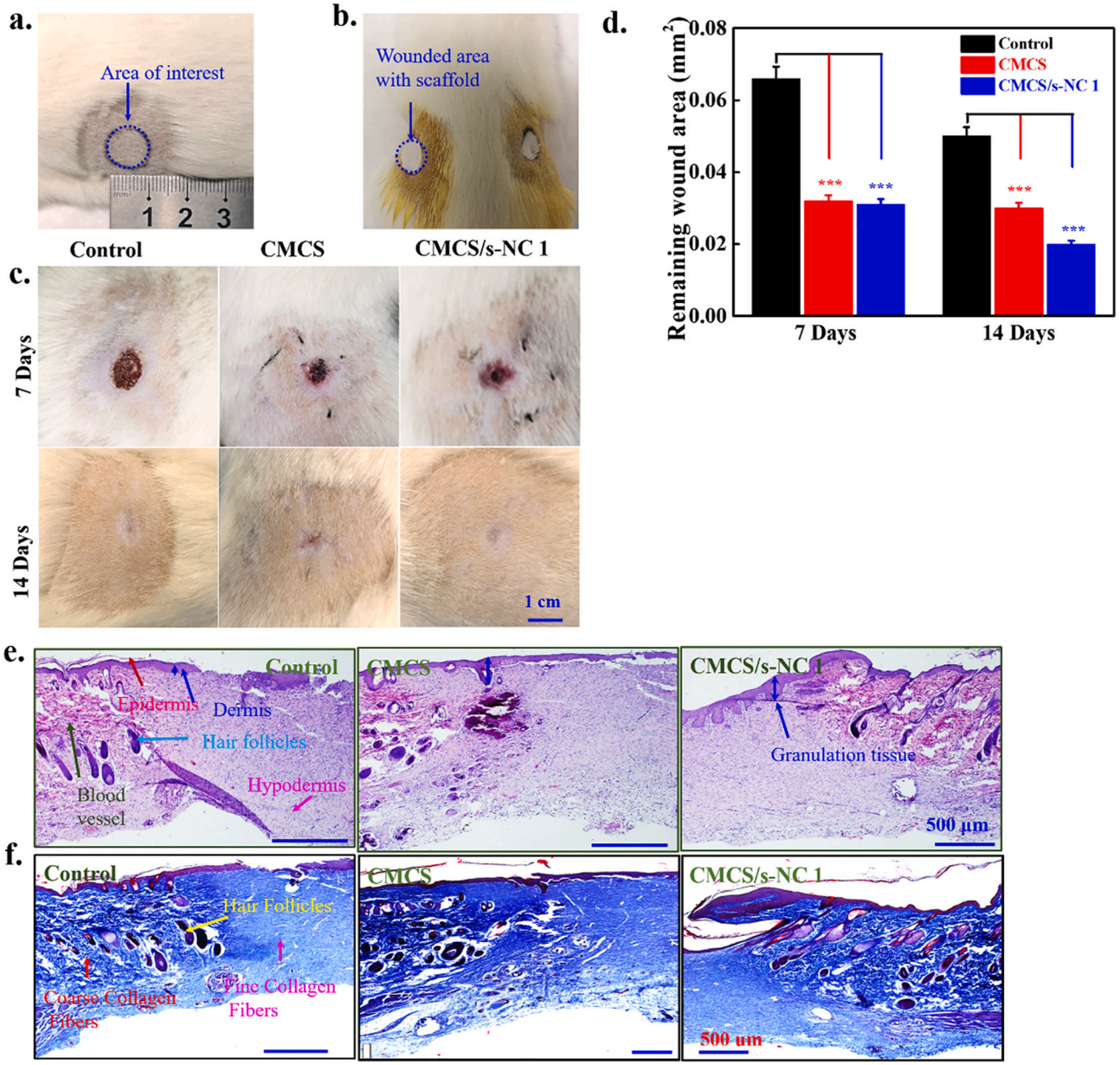


**Fig. 8.** Evaluation wound healing potential of the developed hydrogel scaffolds using 3 weeks olds ICR rats. (a) A representative image of the used rat with the area of interest, (b) Rat with the implanted scaffolds, (c) Photographs of the wounded rats after 7 and 14 days of implantation, (d) Remaining wound area after 7 and 14 days of treatment, (e) H&E, and (f) MT staining of the healed area after 14 days of implantation. The statistical analysis was performed between the control and treated groups (number of wounds = 3, $*p < 0.05$, $**p < 0.01$, and $***p < 0.001$).

were higher in scaffolds treated groups than in control. This was significantly higher in CSCM/s-NC 1 hydrogel scaffolds treated groups, showing its improved regeneration potential. The higher regeneration ability of the CSCM/s-NC 1 hydrogel scaffolds is assigned to its greater expression of different factors, including VEGF, which plays a significant role in angiogenesis. The enhanced expression of VEGF triggers the formation of new blood vessels, assists re-epithelization and collagen synthesis (Qu et al., 2018; Sultana et al., 2021). Fibroblasts have abundant granulation tissue and growth factors. It is possible to monitor the wound healing process by observing granulation tissue thickness (Dong et al., 2017). The granulation tissue thickness was 83.91, 171.31, and 225.5 µm for control, CMCS, and CMCS/s-NC 1 scaffolds, respectively. Thus, CMCS/s-NC 1 scaffolds exhibited improved wound healing efficacy than control, and CMCS scaffolds endorsed granulation tissue thickness. Additionally, collagen deposition was also examined by the MT staining method after 14 days of treatment (Fig. 8f). The collagen deposition occurred in all groups. However, its density was high in the scaffolds treated groups, and this significantly higher in CMCS/s-NC 1 scaffolds treated groups, suggesting its better regeneration potential. A rapid and effective wound healing process would significantly lower medical treatment costs and wound care supplements. These results demonstrated that the application of the developed materials led to rapid cutaneous wound healing.

## 4. Conclusion

The injectable and adhesive hydrogels were developed by incorporating s-NC into the CMCS matrix for rapid subcutaneous wound healing application. The developed hydrogels exhibited improved rheological strength. The hydrogels exhibited thixotropic behavior, and ~85% recovery in viscosity was observed after a high shear rate (1000 $s^{-1}$) deformation. The hydrogel was easily injectable and retained its pre-

designed morphology. Strong interactions made the prepared hydrogels exhibit superior adhesive potential with different surfaces (glass, plastic, rubber, stainless steel, and human skin). The biocompatibility of the developed hydrogel scaffolds was monitored with HDF, HaCaT, and HUVEC individually and co-cultured. No adverse effects were observed on skin cells with the developed hydrogel scaffolds, indicating their biocompatibility. The co-culture method also enhanced skin cell viability, suggesting that the developed hydrogels have an accelerating potential for skin cell regeneration. Higher expression of skin tissue-related gene and protein markers occurred in the developed hydrogel scaffolds than the control. The composite hydrogels demonstrated superior antibacterial potential than the control and the pure polymer hydrogel due to the greater damage to the bacterial cell membrane by electrostatic interaction. The developed hydrogel scaffolds exhibited enhanced wound healing potential compared to the control, which was substantially higher in s-NC added scaffolds. Histological analysis revealed that the development of new tissues occurred in all groups. However, their densities were high in s-NC incorporated scaffolds.

Furthermore, thicker granulation tissue was observed in s-NC added scaffolds, demonstrating its enhanced wound healing efficacy by stimulating granulation tissue thickness. Based on these results, we concluded that the prepared hydrogel scaffolds positively affect skin cell proliferation and can be explored in skin tissue engineering for rapid wound closure.

## Data availability

The data used to support the findings of this study are available from the corresponding author upon request.

## CRediT authorship contribution statement

**Dinesh K. Patel:** Conceptualization, Methodology, Investigations, Visualization, Data curation, Formal analysis, Writing – original draft, Writing – review & editing. **Keya Ganguly:** Investigation. **Jin Hexiu:** Investigation. **Sayan Deb Dutta:** Investigation. **Tejal V. Patil:** Investigation. **Ki-Taek Lim:** Supervision, Funding acquisition, Project administration, Writing – review & editing.

## Declaration of competing interest

The authors declare that they have no known competing financial interests or personal relationships that could have appeared to influence the work reported in this paper.

## Acknowledgments

The Basic Science Research Program supported this work through the National Research Foundation of Korea (NRF) funded by the Ministry of Education (No. 2018R1A6A1A03025582 & 2019R1D1A3A03103828), Republic of Korea.

## Appendix A. Supplementary data

Supplementary data to this article can be found online at https://doi.org/10.1016/j.carbpol.2022.119202.

## References

Abouzeid, R. E., Khiari, R., Beneventi, D., & Dufresne, A. (2018). Biomimetic mineralization of three-dimensional printed alginate/TEMPO-oxidized cellulose nanofibril scaffolds for bone tissue engineering. *Biomacromolecules, 19*, 4442–4452.

Alavi, M., & Nokhodchi, A. (2020). An overview on antimicrobial and wound healing properties of ZnO nanobiofilms, hydrogels, and bionanocomposites based on cellulose, chitosan, and alginate polymers. *Carbohydrate Polymers, 227*, Article 115349.

Azizi Samir, M. A. S., Alloin, F., & Dufresne, A. (2005). Review of recent research into cellulosic whiskers, their properties and their application in nanocomposite field. *Biomacromolecules, 6*, 612–626.

Baran, T., Menteş, A., & Arslan, H. (2015). Synthesis and characterization of water soluble O-carboxymethyl chitosan Schiff bases and Cu(II) complexes. *International Journal of Biological Macromolecules, 72*, 94–103.

Blackstone, B. N., Hahn, J. M., McFarland, K. L., DeBruler, D. M., Supp, D. M., & Powell, H. M. (2018). Inflammatory response and biomechanical properties of coaxial scaffolds for engineered skin in vitro and post-grafting. *Acta Biomaterialia, 80*, 247–257.

Bok, J.-S., Byun, S.-H., Park, B.-W., Kang, Y.-H., Lee, S.-L., Rho, G.-J., Hwang, S.-C., Woo, D. K., Lee, H.-J., & Byun, J.-H. (2018). The role of human umbilical vein endothelial cells in osteogenic differentiation of dental follicle-derived stem cells in in vitro co-cultures. *International Journal of Medical Sciences, 15*, 1160–1170.

Bovone, G., Dudaryeva, O. Y., Marco-Dufort, B., & Tibbitt, M. W. (2021). Engineering hydrogel adhesion for biomedical applications via chemical design of the junction. *ACS Biomaterials Science & Engineering, 7*, 4048–4076.

Brandner, J. M., Wang, H.-M., Chou, Y.-T., Wen, Z.-H., Wang, Z.-R., Chen, C.-H., & Ho, M.-L. (2013). Novel biodegradable porous scaffold applied to skin regeneration. *PLoS ONE, 8*, Article e56330.

Bukzem, A. L., Signini, R., dos Santos, D. M., Lião, L. M., & Ascheri, D. P. R. (2016). Optimization of carboxymethyl chitosan synthesis using response surface methodology and desirability function. *International Journal of Biological Macromolecules, 85*, 615–624.

Cardoso, A. M., de Oliveira, E. G., Coradini, K., Bruinsmann, F. A., Aguirre, T., Lorenzoni, R., Barcelos, R. C. S., Roversi, K., Rossato, D. R., Pohlmann, A. R., et al. (2019). Chitosan hydrogels containing nanoencapsulated phenytoin for cutaneous use: Skin permeation/penetration and efficacy in wound healing. *Materials Science and Engineering: C, 96*, 205–217.

Chen, H., Cheng, R., Zhao, X., Zhang, Y., Tam, A., Yan, Y., Shen, H., Zhang, Y. S., Qi, J., Feng, Y., et al. (2019). An injectable self-healing coordinative hydrogel with antibacterial and angiogenic properties for diabetic skin wound repair. *NPG Asia Materials, 11*, 3–15.

Cheng, M., Qin, Z., Liu, Y., Qin, Y., Li, T., Chen, L., & Zhu, M. (2014). Efficient extraction of carboxylated spherical cellulose nanocrystals with narrow distribution through hydrolysis of lyocell fibers by using ammonium persulfate as an oxidant. *Journal of Materials Chemistry A, 2*, 251–258.

Chia, C., Jeffrey, S. S., & Howe, R. T. (2019). Anomalous hysteresis and current fluctuations in cyclic voltammograms at microelectrodes due to Ag leaching from Ag/AgCl reference electrodes. *Electrochemistry Communications, 105*, Article 106499.

Corin, K. A., & Gibson, L. J. (2010). Cell contraction forces in scaffolds with varying pore size and cell density. *Biomaterials, 31*, 4835–4845.

Croisier, F., & Jérôme, C. (2013). Chitosan-based biomaterials for tissue engineering. *European Polymer Journal, 49*, 780–792.

Cui, C., Shao, C., Meng, L., & Yang, J. (2019). High-strength, self-adhesive, and strain-sensitive chitosan/poly(acrylic acid) double-network nanocomposite hydrogels fabricated by salt-soaking strategy for flexible sensors. *ACS Applied Materials & Interfaces, 11*, 39228–39237.

Dainiak, M. B., Allan, I. U., Savina, I. N., Cornelio, L., James, E. S., James, S. L., Mikhalovsky, S. V., Jungvid, H., & Galaev, I. Y. (2010). Gelatin–fibrinogen cryogel dermal matrices for wound repair: Preparation, optimisation and in vitro study. *Biomaterials, 31*, 67–76.

Dalle Carbonare, L., Mottes, M., Brunelli, A., Deiana, M., Cheri, S., Suardi, S., & Valenti, M. (2019). Effects of oral anticoagulant therapy on gene expression in crosstalk between osteogenic progenitor cells and endothelial cells. *Journal of Clinical Medicine, 8*, 329.

Domingues, R. M. A., Gomes, M. E., & Reis, R. L. (2014). The potential of cellulose nanocrystals in tissue engineering strategies. *Biomacromolecules, 15*, 2327–2346.

Dong, Y., Sigen, A., Rodrigues, M., Li, X., Kwon, S. H., Kosaric, N., Khong, S., Gao, Y., Wang, W., & Gurtner, G. C. (2017). Injectable and tunable gelatin hydrogels enhance stem cell retention and improve cutaneous wound healing. *Advanced Functional Materials, 27*, Article 1606619.

Doshi, B., Repo, E., Heiskanen, J. P., Sirviö, J. A., & Sillanpää, M. (2017). Effectiveness of N, O-carboxymethyl chitosan on destabilization of marine diesel, diesel and marine-2T oil for oil spill treatment. *Carbohydrate Polymers, 167*, 326–336.

Han, L., Yan, L., Wang, K., Fang, L., Zhang, H., Tang, Y., Ding, Y., Weng, L.-T., Xu, J., Weng, J., et al. (2017). Tough, self-healable and tissue-adhesive hydrogel with tunable multifunctionality. *NPG Asia Materials, 9*. e372-e372.

Hunt, N. C., Shelton, R. M., & Grover, L. (2009). An alginate hydrogel matrix for the localised delivery of a fibroblast/keratinocyte co-culture. *Biotechnology Journal, 4*, 730–737.

Keirouz, A., Chung, M., Kwon, J., Fortunato, G., & Radacsi, N. (2020). 2D and 3D electrospinning technologies for the fabrication of nanofibrous scaffolds for skin tissue engineering: A review. In *WIREs Nanomedicine and Nanobiotechnology 12*.

Kendall, R. T., & Feghali-Bostwick, C. A. (2014). Fibroblasts in fibrosis: Novel roles and mediators. *Frontiers in Pharmacology*, 5.

Khodabakhshi, D., Eskandarinia, A., Kefayat, A., Rafienia, M., Navid, S., Karbasi, S., & Moshtaghian, J. (2019). In vitro and in vivo performance of a propolis-coated polyurethane wound dressing with high porosity and antibacterial efficacy. *Colloids and Surfaces B: Biointerfaces, 178*, 177–184.

Korupalli, C., Li, H., Nguyen, N., Mi, F. L., Chang, Y., Lin, Y. J., & Sung, H. W. (2020). Conductive materials for healing wounds: Their incorporation in electroactive wound dressings, characterization, and perspectives. *Advanced Healthcare Materials, 10*, 2001384.

Lima Cunha, D., Oram, A., Gruber, R., Plank, R., Lingenhel, A., Gupta, M. K., Altmüller, J., Nürnberg, P., Schmuth, M., Zschocke, J., et al. (2021). hiPSC-derived

epidermal keratinocytes from ichthyosis patients show altered expression of cornification markers. *International Journal of Molecular Sciences, 22*, 1785.
Liu, H., Wang, C., Li, C., Qin, Y., Wang, Z., Yang, F., Li, Z., & Wang, J. (2018). A functional chitosan-based hydrogel as a wound dressing and drug delivery system in the treatment of wound healing. *RSC Advances, 8*, 7533–7549.
Lord, M. S., Ellis, A. L., Farrugia, B. L., Whitelock, J. M., Grenett, H., Li, C., O'Grady, R. L., & DeCarlo, A. A. (2017). Perlecan and vascular endothelial growth factor-encoding DNA-loaded chitosan scaffolds promote angiogenesis and wound healing. *Journal of Controlled Release, 250*, 48–61.
Lukanina, K. I., Grigoriev, T. E., Krasheninnikov, S. V., Mamagulashvilli, V. G., Kamyshinsky, R. A., & Chvalun, S. N. (2018). Multi-hierarchical tissue-engineering ECM-like scaffolds based on cellulose acetate with collagen and chitosan fillers. *Carbohydrate Polymers, 191*, 119–126.
Luo, H., Cha, R., Li, J., Hao, W., Zhang, Y., & Zhou, F. (2019). Advances in tissue engineering of nanocellulose-based scaffolds: A review. *Carbohydrate Polymers, 224*, Article 115144.
Luo, P., Nie, M., Wen, H., Xu, W., Fan, L., & Cao, Q. (2018). Preparation and characterization of carboxymethyl chitosan sulfate/oxidized konjac glucomannan hydrogels. *International Journal of Biological Macromolecules, 113*, 1024–1031.
Ma, L. (2003). Collagen/chitosan porous scaffolds with improved biostability for skin tissue engineering. *Biomaterials, 24*, 4833–4841.
Ma, M., Zhong, Y., & Jiang, X. (2020). Thermosensitive and pH-responsive tannin-containing hydroxypropyl chitin hydrogel with long-lasting antibacterial activity for wound healing. *Carbohydrate Polymers, 236*, Article 116096.
Mabrouk, M., Beherei, H. H., & Das, D. B. (2020). Recent progress in the fabrication techniques of 3D scaffolds for tissue engineering. *Materials Science and Engineering: C, 110*, Article 110716.
Malakpour-Permlid, A., Buzzi, I., Hegardt, C., Johansson, F., & Oredsson, S. (2021). Identification of extracellular matrix proteins secreted by human dermal fibroblasts cultured in 3D electrospun scaffolds. *Scientific Reports, 11*, 6655–6673.
Nie, W., Yuan, X., Zhao, J., Zhou, Y., & Bao, H. (2013). Rapidly in situ forming chitosan/ε-polylysine hydrogels for adhesive sealants and hemostatic materials. *Carbohydrate Polymers, 96*, 342–348.
Pal, P., Dadhich, P., Srivas, P. K., Das, B., Maulik, D., & Dhara, S. (2017). Bilayered nanofibrous 3D hierarchy as skin rudiment by emulsion electrospinning for burn wound management. *Biomaterials Science, 5*, 1786–1799.
Patel, D. K., Dutta, S. D., Ganguly, K., & Lim, K.-T. (2021). Multifunctional bioactive chitosan/cellulose nanocrystal scaffolds eradicate bacterial growth and sustain drug delivery. *International Journal of Biological Macromolecules, 170*, 178–188.
Patel, D. K., Dutta, S. D., Hexiu, J., Ganguly, K., & Lim, K.-T. (2020). Bioactive electrospun nanocomposite scaffolds of poly(lactic acid)/cellulose nanocrystals for bone tissue engineering. *International Journal of Biological Macromolecules, 162*, 1429–1441.
Patel, D. K., Dutta, S. D., & Lim, K.-T. (2019a). Nanocellulose-based polymer hybrids and their emerging applications in biomedical engineering and water purification. *RSC Advances, 9*, 19143–19162.
Patel, D. K., Seo, Y.-R., Dutta, S. D., & Lim, K.-T. (2019b). Enhanced osteogenesis of mesenchymal stem cells on electrospun cellulose nanocrystals/poly(ε-caprolactone) nanofibers on graphene oxide substrates. *RSC Advances, 9*, 36040–36049.
Pati, F., Jang, J., Ha, D.-H., Won Kim, S., Rhie, J.-W., Shim, J.-H., Kim, D.-H., & Cho, D.-W. (2014). Printing three-dimensional tissue analogues with decellularized extracellular matrix bioink. *Nature Communications, 5*, 3935–3946.
Pei, X., Zhang, H., Zhou, Y., Zhou, L., & Fu, J. (2020). Stretchable, self-healing and tissue-adhesive zwitterionic hydrogels as strain sensors for wireless monitoring of organ motions. *Materials Horizons, 7*, 1872–1882.
Pereira, M. M., Raposo, N. R. B., Brayner, R., Teixeira, E. M., Oliveira, V., Quintão, C. C. R., Camargo, L. S. A., Mattoso, L. H. C., & Brandão, H. M. (2013). Cytotoxicity and expression of genes involved in the cellular stress response and apoptosis in mammalian fibroblast exposed to cotton cellulose nanofibers. *Nanotechnology, 24*, Article 075103.
Piipponen, M., Li, D., & Landén, N. X. (2020). The immune functions of keratinocytes in skin wound healing. *International Journal of Molecular Sciences, 21*, 8790.
Qu, J., Zhao, X., Liang, Y., Zhang, T., Ma, P. X., & Guo, B. (2018). Antibacterial adhesive injectable hydrogels with rapid self-healing, extensibility and compressibility as wound dressing for joints skin wound healing. *Biomaterials, 183*, 185–199.
Schauber, J., Gauglitz, G. G., Zedler, S., v. Spiegel, F., Fuhr, J., v. Donnersmarck, G. H., & Faist, E. (2012). Functional characterization of cultured keratinocytes after acute cutaneous burn injury. *PLoS ONE, 7*, Article e29942.
Sultana, T., Hossain, M., Rahaman, S., Kim, Y. S., Gwon, J.-G., & Lee, B.-T. (2021). Multi-functional nanocellulose-chitosan dressing loaded with antibacterial lawsone for rapid hemostasis and cutaneous wound healing. *Carbohydrate Polymers, 272*, Article 118482.
Tao, L., Zhonglong, L., Ming, X., Zezheng, Y., Zhiyuan, L., Xiaojun, Z., & Jinwu, W. (2017). In vitro and in vivo studies of a gelatin/carboxymethyl chitosan/LAPONITE® composite scaffold for bone tissue engineering. *RSC Advances, 7*, 54100–54110.
Wan, Y., Creber, K. A. M., Peppley, B., & Bui, V. T. (2003). Synthesis, characterization and ionic conductive properties of phosphorylated chitosan membranes. *Macromolecular Chemistry and Physics, 204*, 850–858.
Wang, F., Wang, M., She, Z., Fan, K., Xu, C., Chu, B., Chen, C., Shi, S., & Tan, R. (2015). Collagen/chitosan based two-compartment and bi-functional dermal scaffolds for skin regeneration. *Materials Science and Engineering: C, 52*, 155–162.
Wu, H., Williams, G. R., Wu, J., Wu, J., Niu, S., Li, H., Wang, H., & Zhu, L. (2018). Regenerated chitin fibers reinforced with bacterial cellulose nanocrystals as suture biomaterials. *Carbohydrate Polymers, 180*, 304–313.
Wu, J.-Y., Ooi, C. W., Song, C. P., Wang, C.-Y., Liu, B.-L., Lin, G.-Y., Chiu, C.-Y., & Chang, Y.-K. (2021). Antibacterial efficacy of quaternized chitosan/poly (vinyl alcohol) nanofiber membrane crosslinked with blocked diisocyanate. *Carbohydrate Polymers, 262*, Article 117910.
Wu, R., & Zhu, Z. (2018). Self-powered enzymatic electrosynthesis of l-3,4-dihydroxyphenylalanine in a hybrid bioelectrochemical system. *ACS Sustainable Chemistry & Engineering, 6*, 12593–12597.
Xie, Y., Liao, X., Zhang, J., Yang, F., & Fan, Z. (2018). Novel chitosan hydrogels reinforced by silver nanoparticles with ultrahigh mechanical and high antibacterial properties for accelerating wound healing. *International Journal of Biological Macromolecules, 119*, 402–412.
Xu, X., Liu, F., Jiang, L., Zhu, J. Y., Haagenson, D., & Wiesenborn, D. P. (2013). Cellulose nanocrystals vs. cellulose nanofibrils: A comparative study on their microstructures and effects as polymer reinforcing agents. *ACS Applied Materials & Interfaces, 5*, 2999–3009.
Yang, X., Bakaic, E., Hoare, T., & Cranston, E. D. (2013). Injectable polysaccharide hydrogels reinforced with cellulose nanocrystals: Morphology, rheology, degradation, and cytotoxicity. *Biomacromolecules, 14*, 4447–4455.
Yu, J. R., Navarro, J., Coburn, J. C., Mahadik, B., Molnar, J., Holmes, J. H., Nam, A. J., & Fisher, J. P. (2019). Current and future perspectives on skin tissue engineering: Key features of biomedical research, translational assessment, and clinical application. *Advanced Healthcare Materials, 8*, 1801471.
Yuan, H., Chen, L., & Hong, F. F. (2019). A biodegradable antibacterial nanocomposite based on oxidized bacterial nanocellulose for rapid hemostasis and wound healing. *ACS Applied Materials & Interfaces, 12*, 3382–3392.
Zhang, C., Yang, X., Li, Y., Qiao, C., Wang, S., Wang, X., Xu, C., Yang, H., & Li, T. (2020). Enhancement of a zwitterionic chitosan derivative on mechanical properties and antibacterial activity of carboxymethyl cellulose-based films. *International Journal of Biological Macromolecules, 159*, 1197–1205.
Zhang, L., Wang, L., Guo, B., & Ma, P. X. (2014). Cytocompatible injectable carboxymethyl chitosan/N-isopropylacrylamide hydrogels for localized drug delivery. *Carbohydrate Polymers, 103*, 110–118.
Zhang, X.-Y., Chen, Y.-P., Han, J., Mo, J., Dong, P.-F., Zhuo, Y.-H., & Feng, Y. (2019). Biocompatiable silk fibroin/carboxymethyl chitosan/strontium substituted hydroxyapatite/cellulose nanocrystal composite scaffolds for bone tissue engineering. *International Journal of Biological Macromolecules, 136*, 1247–1257.
Zhao, X., Guo, B., Wu, H., Liang, Y., & Ma, P. X. (2018). Injectable antibacterial conductive nanocomposite cryogels with rapid shape recovery for noncompressible hemorrhage and wound healing. *Nature Communications, 9*, 2784–2801.